aerospace

MDPI

*Article*

# Static Geotechnical Characterization of Lunar Soil Simulants

**Devansh Joshi [1], Timothy Newson [1,*] and Gordon R. Osinski [2]**

[1] Department of Civil and Environmental Engineering, University of Western Ontario, 1151 Richmond St, London, ON N6A 3K7, Canada; djoshi28@uwo.ca
[2] Department of Earth Sciences, University of Western Ontario, 1151 Richmond St, London, ON N6A 3K7, Canada; gosinski@uwo.ca
* Correspondence: tnewson@eng.uwo.ca; Tel.: +1-519-880-2973

**Abstract**

Recent technological advances and the reinvigoration of NASA's Artemis program have increased the feasibility of lunar habitats and supporting infrastructure, necessitating the development of specialized foundation systems capable of maintaining stability under transferred structured loads. Site investigation techniques, including in situ testing, sampling, and geophysical mapping, must therefore be adapted for lunar conditions, while construction using regolith requires an improved understanding of lunar soil mechanics. Foundations must also endure extreme thermal fluctuations, reduced gravity, radiation exposure, micrometeoroid impacts, and lunar seismicity to ensure long-term performance. Consequently, enhanced knowledge of the monotonic and cyclic geotechnical behavior of lunar soils is essential. Owing to the limited availability of in situ testing opportunities and returned lunar materials, high-fidelity simulants that replicate regolith behavior are required for experimental studies. This research investigates the static behavior of several contemporary lunar simulants and compares their responses with terrestrial benchmark soils. The results indicate that the overall stress–strain trends of lunar simulants broadly resemble those of terrestrial soils; however, the particle morphology and distinctive mineralogical compositions, including basaltic and anorthositic constituents, yield higher values of certain geomechanical parameters. Comparison with terrestrial datasets further suggests that carefully selected benchmark soils may facilitate the development of a next generation of lunar simulants with improved fidelity to lunar regolith.

**Keywords:** static; geomechanical; regolith; lunar simulants; stress–strain; strength; friction angle; compressibility; particle shape; particle size distribution

Check for updates

Academic Editor: M. Reza Emami

Received: 31 March 2026
Revised: 25 May 2026
Accepted: 29 May 2026
Published: 4 June 2026



## 1. Introduction

After relatively little interest in the decades after the Apollo program, there is renewed interest and investment in the exploration of the Moon, as evidenced by the NASA-led Artemis program and China's Lunar Exploration Program. Lunar exploration serves as more than just a standalone objective; it is also envisioned to be a vital stepping stone for further space and interplanetary exploration. Of particular importance for current missions is the existence and distribution of polar ice on the Moon [1]. Consequently, nations such as Canada, the USA, China, India, Japan, Korea, and the European Union are beginning to pay much closer attention to the study of the mechanical characteristics of lunar regolith (soil), since recent technological advances have made proposals for lunar habitats, storage facilities, support structures, and transportation infrastructure more feasible [2]. These necessary structures are both surface- and sub-surface-based, and, since they all interact with the lunar surface and materials, they will require the development of suitable foundations and sub-base layers for the safe transfer of structural loads to ensure adequate stability and support (e.g., [3]). The requisite precursor site investigation and geotechnical material characterization methods (e.g., in situ testing, sampling, and geophysical mapping) [4] will also need modification for lunar deployment. Any surface or sub-surface construction involving regolith (e.g., shallow or deep excavation, pavements/landing pads/embankments and other fills, slope stabilization/modification, and the sourcing of materials for construction) will require greater insights intoand knowledge of lunar soil stratigraphy and regolith mechanics (over a range of stresses and packing states) than we currently possess (e.g., [4,5]). Supporting foundation structures will also need to perform adequately in the long term when subjected to unfamiliar challenges in terms of large temperature variations, different atmospheric conditions, lower gravity, higher radiation exposure, micrometeoroid impacts, and lunar seismicity [2,3,6].

It is well known that lunar regolith samples are currently not available in sufficient quantities for such detailed soil mechanics studies and thus the ongoing development of lunar regolith simulants has been significant. Lunar simulants are defined as materials manufactured from natural or synthetic terrestrial or meteoritic components for the purpose of simulating one or more physical and/or chemical properties of lunar rock or soil [7]. Terrestrial materials specifically chosen to simulate lunar regolith need to be processed appropriately to replicate critical physical and chemical/mineralogical parameters; they may also have other added components, such as synthetic materials (i.e., glasses, metals, and minerals), to provide some of the unique qualities of lunar regolith [7,8]. Lunar regolith is composed of materials that are predominantly basaltic and anorthositic, reflecting mare (LM) and highland (LH) source regions, respectively. Meteorite impacts and space weathering events have blended these materials over large areas of the lunar surface and have produced significant fragmentation, melting, and glass formation. These actions are evident in the texture, chemistry, mineralogy, and presence of significant glass fractions in the lunar regolith, as well as vapor-deposited reduced iron, also known as nanophase iron. Lunar simulants can, in principle, be matched to lunar source materials by means of selecting root components that, when mixed and processed appropriately, duplicate the characteristics of lunar target materials. Potential root materials (herein defined as terrestrial soils or rocks that are used for simulant development by modifying their base characteristics to target the required lunar regolith characteristics) for simulants include basalt, anorthosite, mineral and glass separates, and small size fractions, such as dust and Fe nanophase material. Based on trace element chemistry, meteoritic material exists in lunar regolith and represents a challenge in identifying equivalent terrestrial materials to use as simulants [9].

To date, there have been more than 30 different types of lunar regolith simulants developed since the Apollo program for use with exploration missions in various scientific and engineering applications. Understanding the soil (regolith) mechanic characteristics of lunar simulants is vital to judge the quality and performance of simulants compared to lunar regolith. Simple material characteristics, including the bulk and surface chemistry, particle shape, size and distribution, specific gravity, density, surface texture, and voids, affect the static and dynamic mechanical behavior of these simulants. A number of researchers have investigated these aspects and other fundamental characteristics of lunar simulants [10–17]. Where the stress–strain behavior has been investigated (e.g., [18–21]), these efforts have concentrated on basic monotonic loading tests (commonly referred to as 'static' tests in the civil engineering literature), where the loads are steadily increased until failure (or other defined threshold states are reached). In comparison, cyclic (dynamic) testing of regolith or simulants, with a repeated pattern of closed loading and unloading

https://doi.org/10.3390/aerospace13060527

cycles, is almost absent from the literature. Both forms of soil stress–strain testing protocols are prescribed by standards organizations for terrestrial materials (e.g., ASTM) and are commonly used to determine strength, stiffness and other characteristics of soils for use by geotechnical engineers. However, in contrast to terrestrial soils, complex stress–strain investigations, more nuanced soil mechanics interpretations (e.g., critical state soil mechanics: [22,23]), and extensive databases of mechanical behaviors are not currently available for regolith simulants.

The majority of the aforementioned lunar simulants available for research and commercial purposes are very similar to terrestrial silty sands/clean sands (i.e., sand grains [0.075 mm–4.75 mm sized] with and without silt [0.075 mm–0.002 mm] particles) based on their particle size distributions. The elastic moduli of these terrestrial materials are dependent on the void ratio and relative density, as noted by many studies (e.g., [24–26]). Additionally, the strength and stiffness also depend on the gradation, particle shape, and confining pressure [25,27–29]. Some of these findings have been generally confirmed for a narrow number of simulants (e.g., [11,15,18,19]), with some cross-comparison of a limited range of geotechnical attributes between the different simulants. In addition, comparison of the particle size distributions of lunar regoliths [5] suggest that a number of lunar simulants have narrower ranges of particle size (classified with the USCS standard soil system as poorly graded, with coefficient of uniformity $C_u < 6$ and coefficient of curvature $C_z < 1$) [17], which is due to the preparation methods employed.

A comprehensive body of soil mechanics data exists for both terrestrial silty sands and clean sands (with narrower gradings), often based on standard ‘benchmark’ materials (e.g., Toyoura, Ottawa and Hostun Sand). Studies of the static behavior of silty sands demonstrate common trends of changes in strength and stiffness with variations in the percentage of fines [30]. The transition in the behavior of soils from sand-dominant responses to silt-dominant responses gradually occurs with fines content in the range of 10–25% [30]. The particle mineralogy also influences the stress–strain response and compressibility of sandy soils. Ref. [31] observed that the presence of quartz in sandy soils triggers a dilative response at intermediate shear strain levels, leading to higher mobilized friction angles, while the presence of more compressible albite minerals in sandy soil tends to induce contractive behavior at all shear strain levels at a higher initial relative density. The compressibility index $C_c$ and shear modulus G are also found to increase with an increase in particle angularity for sands [32]. Ref. [33] also suggested that particle shape effects are more distinctly observed in loose compaction states compared to dense states.

Given the similarity of these terrestrial materials to lunar regolith and simulants, lunar materials are likely to perform mechanically (under static loads) in a similar way. However, with distinct deviations in particle shape and mineralogy, there are expected to be some differences. The extent of the potential variations has not yet been determined and reported in published studies. Therefore, the main objective of this research project was to investigate the static stress–strain behavior of a group of well-known lunar simulants, linking this behavior to a range of geotechnical attributes and comparing this database to those for some benchmark terrestrial soils. These geomechanical characterizations include stress–strain parameters such as cohesion, the peak and critical-state friction angle, the dilation angle, and 1D compression and swelling indices, as well as basic index properties such as—particle shape, particle size distribution, grain density and limit (physically possible) packing states—which are very important when considering static (monotonic) loading from potential lunar infrastructure and other lunar construction activities.

## 2. Materials and Testing

A range of different types of regolith analogs were used in this research, which included seven lunar simulants, a Martian simulant (MMS-MG), a benchmark terrestrial soil (Toyoura Sand—TS), and an artificial terrestrial soil mixture (silica silt and Toyoura sand—AM). The seven lunar simulants (CAS-1, EAC-1, OPRL2N, OPRH2N, LHS-1, LMS-1, and OB-1A) are commonly cited and have been developed by various space agencies and companies to support their lunar exploration programs, and they cover both lunar mare (LM) and lunar highland (LH) materials. In-depth descriptions of these materials and their characteristics are provided in other works, e.g., [17], and only a brief overview of the different materials is presented in Table 1.

**Table 1.** Overview of the materials used in the research.

| Material Ref. | Name | Manufactured/ Developed at | Country | Target Region | Description |
|---|---|---|---|---|---|
| 1 | CAS-1 [34] | Chinese Academy of Sciences, Beijing | China | Lunar Mare | Developed to support China's Lunar Exploration Program's lunar orbiter, soft-landing mission, and sample return missions, which were expected to take place between 2004 and 2020. |
| 2 | EAC-1 | European Astronaut Center, Cologne | Germany | Lunar Mare | The European Astronaut Center (EAC) created the EAC-1 lunar simulant as a lunar testbed regolith at LUNA, a 900 $m^2$ testing facility at EAC [12]. |
| 3 | OPRL2N | Off Planet Research, Everett, WA | USA | Lunar Mare | OPRL2N, a general-purpose mare simulant, has enhanced fidelity, and the particle size distribution was intended to be comparable to those of returned Apollo-17 samples. |
| 4 | OPRH2N | Off Planet Research | USA | Lunar Highland | A lighter-colored highland simulant OPRH2N was developed, similar to OPRL2N, with contrasting proportions of basalt and anorthosite regarding OPRL2N. |
| 5 | LHS-1 | Class Exolith Lab, Orlando, FL | USA | Lunar Highland | A general-purpose, high-fidelity highland simulant was developed with a particle size distribution matching those of soils from the Apollo missions. |
| 6 | LMS-1 [35] | Class Exolith Lab | USA | Lunar Mare | A general-purpose, high-fidelity mare simulate with more nuanced mineralogy than LHS-1; it is a highland counterpart. |
| 7 | OB-1A [11] | Deltion Innovation Ltd., Sudbury, ON | Canada | Lunar Highland | OB-1A, a reproduced version of the OB-1 simulant, was derived from the Kapuskasing Structural Zone in Ontario, Canada. |

https://doi.org/10.3390/aerospace13060527

**Table 1.** *Cont.*

| Material Ref. | Name | Manufactured/ Developed at | Country | Target Region | Description |
|---|---|---|---|---|---|
| 8 | MMS-MG | Martian Garden, Austin, TX | USA | Mars | MMS-MG, a commercially available Martian simulant, was developed using high-quality, iron-rich basalt from the same region as that used by scientists of NASA (Jet Propulsion Laboratory, NASA) to develop MMS. |
| 9 | Toyoura Sand (TS) | Toyoura Keiseki Kogyo Co., Ltd., Yamaguchi | Japan | Terrestrial Benchmark Soil | A fine-grained, poorly graded sand (SP) with a subangular to angular particle shape. It is a standard sand produced under JIS R 5201 [36] and has become a benchmark terrestrial soil for geotechnical engineers. |
| 10 | Artificial Mix (AM) | Western University, London, ON | Canada | Artificial Terrestrial Soil | This mix was prepared by adding Toyoura Sand and Sil-Co-Sil 106 (fine-grained, well-graded [ML] powdered quartz) at a ratio of 2:1 to create a soil with a wider range of particle sizes and a finer average particle size, more comparable to the lunar simulants. |

The particle mineralogy influences many geotechnical properties and hence the mineralogical fidelity of simulants to lunar regolith is very important. The mineralogy of the simulants and soils used is presented in Table 2. Evident from Table 2 are the higher concentrations of anorthosites and plagioclase feldspar in the LH simulants, demonstrating mineralogical fidelity to the highland regions compared to the mare regions. However, it should be noted that the mineral chemistry of most simulants is poorly documented. While the LHS-1 and LMS-1 simulants were developed specifically as mineral-based simulants and contain glass-rich basalt [35], which resembles lunar regolith, the composition of the plagioclase in LMS-1 is not provided; the plagioclase in LHS-1 is listed as anorthite, which would suggest $> An_{90}$. The mineralogy of EAC-1 is from the sourced basaltic unit and not the simulant itself, while the mineralogy of CAS-1 does not account for its glass content. OB-1A represents one of the best-characterized simulants from this perspective. The composition of the plagioclase includes an anorthite number of $An_{78}$—which, as the authors note, is not as high as that of lunar plagioclase (typically $> An_{90}$) but is much higher than those of most terrestrial anorthosites (typically $An_{50–70}$) [32]. Further discussion of the mineralogies of CAS-1, LMS-1, and OB-1A can be found in [11,34,35], and it is anticipated that the variations in the compositions of the plagioclase will likely influence the mechanical behavior [37]. In comparison, the two terrestrial soils (TS and AM) are primarily quartz (although TS has some alkali feldspar), and MMS-MG has a predominantly plagioclase mineralogy.

### *2.1. Material Testing*

Various types of geotechnical tests were conducted on the different regolith simulants and soils to evaluate their index properties, mineralogy and structures, and geomechanical stress–strain characteristics. Scanning electron microscopy (SEM) was also used to determine shape parameters, and X-ray diffraction (XRD) was used to understand the bulk chemistry. These XRD data are analyzed and described elsewhere [38].

**Table 2.** Mineralogy of simulants and benchmark terrestrial soils.

| Mineral | Lunar Mare Simulants | | | | Lunar Highland Simulants | | | Terrestrial Soils | | Martian Simulant |
|---|---|---|---|---|---|---|---|---|---|---|
| | CAS-1 | EAC-1 | OPR L2N | LMS-1 | LHS-1 | OPR H2N | OB-1A | Toyoura Sand | Sil-Co-Sil 106 | MMS-MG |
| Anorthosite | - | - | 10 | - | - | - | - | - | - | - |
| Apatite | 0.65 | - | - | - | - | 0.02 | - | - | - | - |
| Basalt | - | 100 | 90 | 8 | - | - | - | - | - | - |
| Diopside | 7.74 | - | - | - | - | 0.18 | - | - | - | - |
| Alkali feldspar | 7.24 | - | - | - | - | 1.02 | <0.5 | 22 | - | - |
| Basaltic glass | - | - | - | 25 | 24 | - | - | - | - | - |
| Slag glass | - | - | - | - | - | - | 42 | - | - | - |
| Gypsum | | | | | | | | | - | 10.8 |
| Hematite | | | | | | | | | - | 1.7 |
| Hypersthene | 14.60 | - | - | - | - | 0.41 | - | - | - | - |
| Ilmenite | 2.33 | - | - | 4 | 0.4 | 0.06 | - | - | - | - |
| Magnetite | 3.03 | - | - | - | - | 0.07 | - | - | - | - |
| Magnetite | - | - | - | - | - | - | - | 3 | - | - |
| Olivine | 8.18 | - | - | 11 | 0.3 | 1.11 | - | - | - | - |
| Plagioclase | 56.23 | - | - | 20 | 74 | 97.13 | 57 | - | - | 87.4 |
| Pyroxene | - | - | - | 38 | 0.2 | - | <0.5 | - | - | - |
| Quartz | - | - | - | - | - | - | - | 75 | 100 | 0.1 |

The index property tests included particle size distribution (ASTM D6913, D7928) [39,40], specific gravity (ASTM D854) [41], and maximum and minimum dry density tests (ASTM D4253, D4254) [42,43], which were all conducted to the named standards. The geomechanical tests included direct shear tests to determine shear strength parameters [cohesion and angle of friction] (ASTM D3080) [44] and oedometer tests (ASTM D2435-04) [45] to determine compression responses under 1D loading. Characterization of the soils was based on the USCS standard for soil classification (ASTM D-2487) [46].

### *2.2. Particle Shape Analysis*

The particle shape is one of the most important characteristics influencing lunar regolith mechanics behavior [5]. The simulants and terrestrial soils were imaged using scanning electron microscopy (SEM) in the University of Western Ontario Department of Physics and Astronomy's nanofabrication laboratory. To analyze the simulants, a Zeiss LEO 1540 XB field emission SEM device was utilized. For the SEM analysis, less than 10 g of simulant was needed, and contamination was avoided. Carbon sputtering was used on the imaging stubs to reduce the electrical charge of the surface particles, leading to accurate images. High-resolution images were captured at various magnifications, and these were used for image analysis to determine the roundness (R), sphericity (S), and regularity ($R_g$) of the particles.

Particle image analysis was conducted using the ImagePro 10 software, and at least 40 particles of each soil were examined. Sphericity and roundness were calculated from the average particle dimensions using Equations (1) and (2) [47]. Sphericity (S) relates to the global form of the particle (i.e., eccentricity or platiness) and reflects the similarity between the particle's lengths in three mutually perpendicular directions. This parameter is characterized using the diameter of the largest inscribed sphere relative to the diameter of the smallest circumscribed sphere. Roundness (R) relates to the scale of any major particle surface features (i.e., angularity) and is quantified as the average radius of curvature of surface features relative to the radius of the maximum sphere that can be inscribed in the particle. In addition, regularity ($R_g$) is calculated using the average of sphericity and roundness (=[S + R]/2) and can be used as another measure of particle deviation from a 'round spherical' shape.

$$Sphericity\ (S) = \frac{r_{(max-in)}}{r_{(min-cir)}} \tag{1}$$

$$Roundness\ (R) = \frac{\Sigma r_i/N}{r_{(max-in)}} \tag{2}$$

where $r_{max}$ = maximum radius of a circle within a soil particle, $r_{min}$ = minimum radius of a circle within a soil particle, $r_{in}$ = radius of the incircle of the soil particle, $r_{cir}$ = radius of the circumcircle of the soil particle, and N = number of circles etched within a soil particle.

### *2.3. Stress–Strain Tests*

All of the stress–strain testing was conducted with dry materials in a temperature- and humidity-controlled laboratory (23 ± 2 °C and RH 50 ± 10%). The oedometer test was conducted as per [45] for all lunar simulant and soil samples. The applied stresses used in the oedometer tests were from 10 to 640 kPa for loading and vice versa for unloading. A series of direct shear tests were also performed on the different material samples using the procedure described in [44]. All samples were tested in a standard direct shear box with cross-sectional dimensions of 6 cm × 6 cm and a nominal initial sample height of 2 cm. The tests were performed at a horizontal strain rate of 0.3 mm/min, under different normal applied stresses from 25 to 200 kPa, respectively. The direct shear tests for simulant samples were performed at different relative densities ($D_r$) of 30% and 60% to determine the simulant behavior and shear strength parameters in loose and medium–dense states. The relative density ($D_r$) is defined in Equation (3) and is commonly used to characterize the current relative packing state in relation to the possible limits (either density or packing states) of a particular soil [48].

$$D_r = \frac{e_{max} - e_{current}}{e_{max} - e_{min}} = \frac{\rho_{current} - \rho_{min}}{\rho_{max} - \rho_{min}} \tag{3}$$

where $e_{current}$ is the current void ratio, $e_{min}$ is the minimum void ratio, $e_{max}$ is the maximum void ratio, $\rho_{current}$ is the current density, $\rho_{min}$ is the minimum density, and $\rho_{max}$ is the maximum density.

## 3. Testing Results

### *3.1. Index Properties*

The grain size distributions of all of the lunar simulants, MMS-MG, TS, and the AM, were derived using a combination of sieve analysis and hydrometer tests using ASTM standard methods [39,40], and Figure 1 shows the resulting grain size distributions for all of the tested materials.

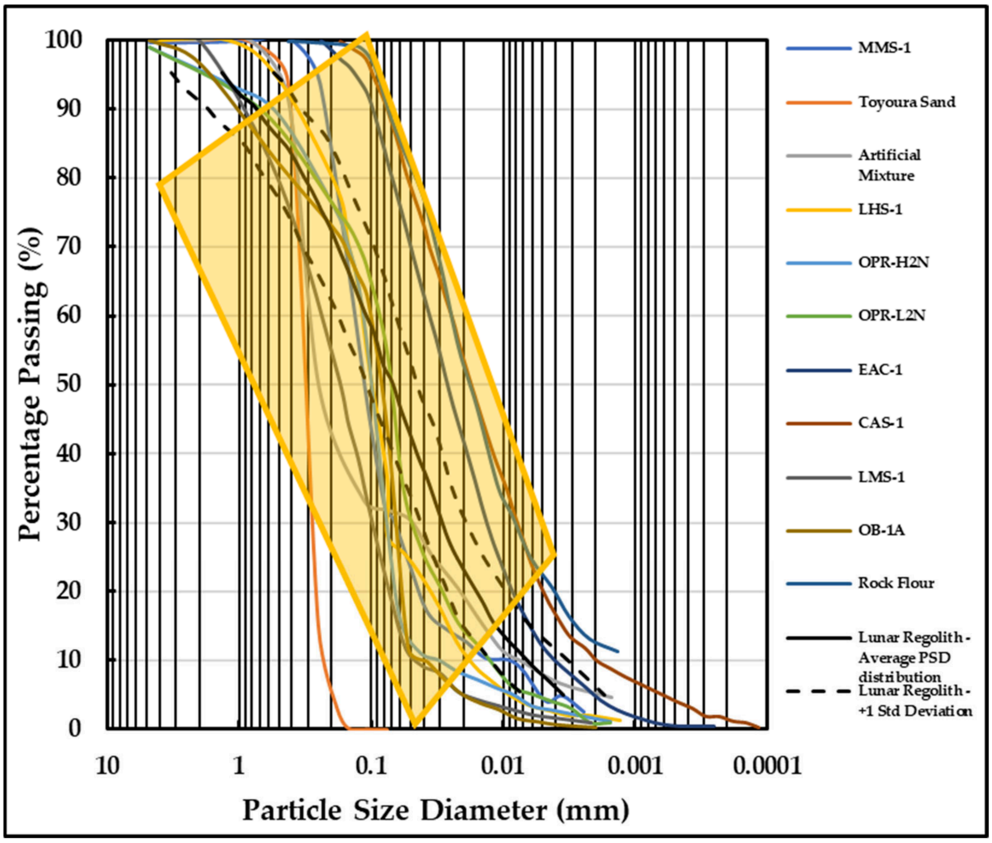


**Figure 1.** Grain size distributions for all tested simulants and soils. Yellow shading covers the range of particle size distributions found from the Apollo missions.

Also shown in Figure 1 is an envelope (shaded yellow) of all of the particle distributions found from the Apollo missions for different lunar regoliths [5]. Based on the particle size distributions in Figure 1, the range of median particle diameters ($D_{50}$) for the lunar simulants varies from 0.018 to 0.18 mm (also see Table 3). The average $D_{50}$ of the lunar soil is 0.072 [5], which is closest to the OPRL2N lunar simulant (0.07). The MMS-MG and two terrestrial soils have coarser mean particle sizes. The average coefficient of uniformity ($C_u = D_{60}/D_{10}$; where $D_{60}$, $D_{10}$ = particle diameters at which 60% and 10% of the soil particles are finer) for lunar regolith is 16, while the $C_u$ value for the lunar simulants is less than 10, with CAS-1 being an exception. This result agrees with other research findings, where lunar simulant $C_u$ values were found to be less than those for lunar regolith [49]. This indicates that the gradation of lunar simulants is generally more uniform compared to the well-graded (wider range of grain sizes) lunar regolith. The particle size distributions (PSDs) of the lunar simulants are likely influenced by the crushing processes of the source material and the targeted Apollo soil samples. These factors tend to produce more uniform PSDs compared to heterogenous lunar soils. On average, the $C_u$ values of the LM simulants are higher as compared to LH simulants. The average coefficient of curvature [$C_z = (D_{30})^2/(D_{60} \cdot D_{10})$, where $D_{60}$, $D_{30}$ = particle diameters at which 60%, 30% of the soil particles are finer; $D_{10}$ = effective particle size] value for lunar soil is in the range of 1–2.8 [11], while the $C_z$ values for lunar simulants fall in the range of 0.48–2.37. Based on the USCS standard for soil classification (ASTM D-2487) [46], all of the tested lunar simulants are classified as silty sand (SM). In comparison, for the terrestrial soils, the $C_u$ values of TS (2.1) and AM (3.87) fall within the range for the lunar simulants, while the $C_z$ values of TS (1.06) and the AM (0.11) are in the lower range of $C_z$ values for the lunar simulants. The MMS has the second-highest $C_u$ value of 10.

**Table 3.** Basic properties of lunar simulants, MMS-MG, and terrestrial soils.

| Soil Type | EAC-1 | OPR L2N | LMS-1 | CAS-1 | OB-1A | OPR H2N | LHS-1 | MMS-MG | Toyoura Sand | Artificial Mix |
|---|---|---|---|---|---|---|---|---|---|---|
| Specific gravity, $G_s$ | 3.07 | 2.9 | 2.9 | 2.74 | 3.01 | 2.9 | 2.73 | 2.67 | 2.65 | 2.65 |
| Maximum dry density, $\rho_{max}$ (g/cc) | 2.03 | 1.84 | 1.96 | 1.65 | 2.01 | 1.85 | 1.87 | 1.53 | 1.65 | 1.95 |
| Minimum dry density, $\rho_{min}$ (g/cc) | 1.51 | 1.38 | 1.53 | 1.3 | 1.45 | 1.37 | 1.31 | 1.18 | 1.34 | 1.41 |
| Initial void ratio ($D_r$—30%) | 0.99 | 1.1 | 0.526 | 1.09 | 0.72 | 1.17 | 0.756 | 1.08 | 0.895 | 0.779 |
| Initial void ratio ($D_r$—60%) | 0.457 | 0.63 | 0.456 | 0.723 | 0.565 | 0.622 | 0.618 | 0.92 | 0.74 | 0.568 |
| Compressibility index ($C_c$) ($D_r$—30) | 0.094 | 0.081 | 0.08 | 0.102 | 0.101 | 0.1 | 0.111 | 0.109 | 0.04 | 0.09 |
| Compressibility index ($C_c$) ($D_r$—60) | 0.085 | 0.075 | 0.066 | 0.066 | 0.075 | 0.105 | 0.093 | 0.096 | 0.035 | 0.076 |
| Uniformity Coefficient, $C_u$ | 9 | 6.53 | 4.8 | 12.5 | 2.22 | 1.2 | 6.41 | 10 | 2.1 | 3.87 |
| Curvature coefficient, $C_z$ | 1.36 | 2.26 | 0.8 | 1.22 | 0.91 | 0.48 | 2.37 | 2.03 | 1.06 | 0.11 |
| Mean particle size, $D_{50}$ (mm) | 0.026 | 0.07 | 0.18 | 0.018 | 0.082 | 0.03 | 0.1 | 0.12 | 0.31 | 0.26 |
| Sphericity (S) | 0.51 | 0.57 | 0.61 | 0.67 | 0.61 | 0.55 | 0.59 | 0.58 | 0.58 | 0.52 |
| Roundness (R) | 0.52 | 0.43 | 0.49 | 0.49 | 0.55 | 0.45 | 0.49 | 0.38 | 0.49 | 0.51 |
| Regularity ($R_g$) | 0.51 | 0.5 | 0.55 | 0.58 | 0.58 | 0.5 | 0.54 | 0.48 | 0.53 | 0.52 |
| $C_c/C_r$ ($D_r$ = 30%) | 10.4 | 8.1 | 11.4 | 12.8 | 16.8 | 3 | 15.9 | 3.8 | 1.5 | 2.5 |
| $C_c/C_r$ ($D_r$ = 60%) | 3.5 | 2.2 | 2.2 | 2.8 | 2.4 | 5 | 2.8 | 3.1 | 1.3 | 2.1 |

In geotechnical terms, the specific gravity ($G_s$) of a soil particle is defined as the ratio of its mass to the mass of an equal volume of water at 4 °C. The specific gravity ($G_s$) of the particles was determined as per [41] for all of the materials. From previous studies, the specific gravity of lunar regolith spans a range of 2.9 to 3.5, and, for engineering design purposes, $G_s$ of 3.1 is recommended [48]. The $G_s$ values of all of the tested materials varied from 2.64 to 3.07, as shown in Table 3.

The limit packing states—i.e., the physically possible maximum and minimum dry densities (associated with $e_{max}$ and $e_{min}$) of the materials (characterizing the soil assemblage, i.e., particles plus voids)—were determined as per [42,43]. The values of maximum density ($\rho_{max}$) and minimum density ($\rho_{min}$) varied from 1.53 to 2.03 g/cc and 1.18 to 1.53 g/cc, respectively, and were used to determine the values of the minimum void ratio ($e_{min}$) and maximum void ratio ($e_{max}$) used for sample preparation, and these are also shown in Table 3. The void ratio (e) is defined as the ratio of the volume of voids to the volume of solids for a soil mass.

The limits of the void ratios ($e_{max}$ and $e_{min}$) for the lunar simulants range from 0.46 to 1.12. This range is lower than the corresponding values for lunar regolith [5]. The values of $e_{max}$ and $e_{min}$ for nine lunar simulants (other than the ones studied in this research) provided in the literature range from 0.33 to 1.76 [17]. The maximum and minimum void ratios are shown in Figure 2. The MMS-MG, TS, and AM have comparable limit packing states to the simulants.

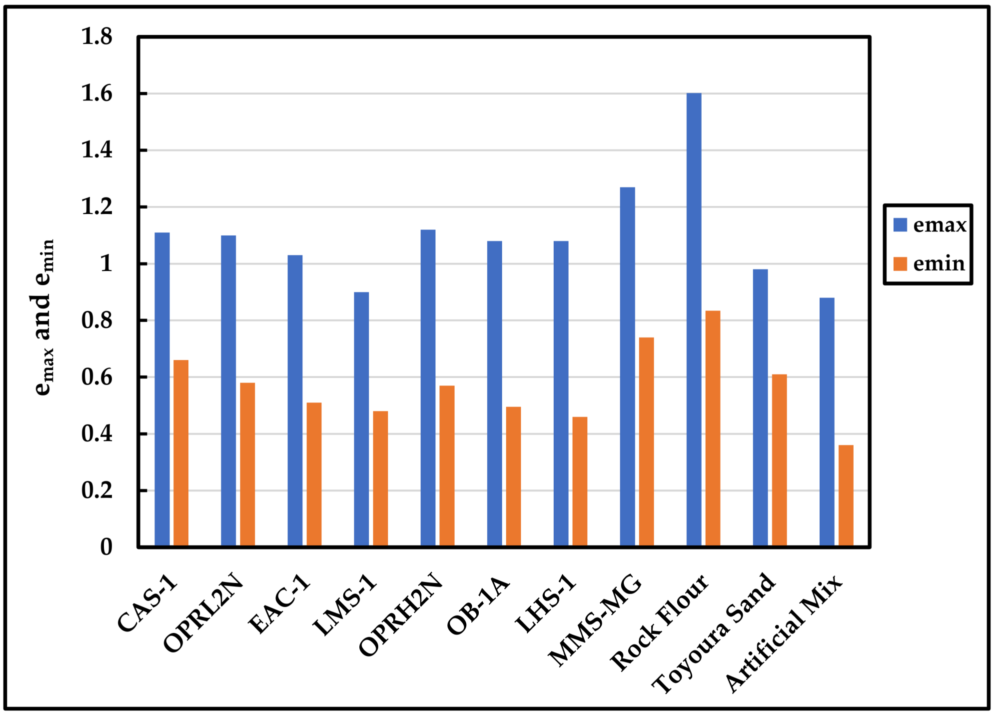


**Figure 2.** Maximum and minimum void ratios of lunar simulants, Martian simulants, and terrestrial soils.

### *3.2. Scanning Electron Microscopy and Shape Analysis*

Figures 3–5 show SEM images of the various simulants and terrestrial soils and broadly show the particle shapes and fabrics. Also shown in the SEM images are different image scales of 10–20 μm to help identify the relative sizes of the different materials. The CAS-1 simulant generally shows angular to subangular particle shapes and uniformity among the particle shapes. The EAC-1 simulant shows a majority of subrounded to rounded particle shapes with a few subangular particles. EAC-1 also shows fine roughness in the texture of the particles. OPRH2N shows a mix of subangular to subrounded particles. LHS-1 shows a majority of angular to subangular particles, while the image of LMS-1 shows a lower spread of particle sizes, with a majority of subangular particles. The Toyoura sand has subangular or angular-shaped grains. Both MMS-MG and the silica flour (Sil-Co-Sil, S = 0.4 and R = 0.56) have angular-shaped grains, which [17,50] attributed to their manufacturing processes. On average, these terrestrial soils are angular to subangular with uniformity in particle shape, while the lunar simulants seem to have a more diverse range of particle shapes.

Further insight is provided through the characterization of the average particle shape parameters, S and R, from the SEM images. The values of these shape parameters are shown in Figure 6 and Table 3 for the lunar simulants (S = 0.51–0.61, R = 0.43–0.54), the natural Toyoura sand (S = 0.58, R = 0.49), and the crushed terrestrial material (MMS-MG), which has S = 0.58 and R = 0.38. These values can be compared to the shape analysis conducted in [51], which investigated both lunar regolith particles from Apollo 11 and 14 and JSC-1A simulant particles using X-ray computed tomography. The authors found that the lunar regolith had average values of S = 0.64 and the JSC-1A had an average of S = 0.62, which is similar to those provided in [52]. These values also lie in a similar range to those found for the lunar simulants in this study.

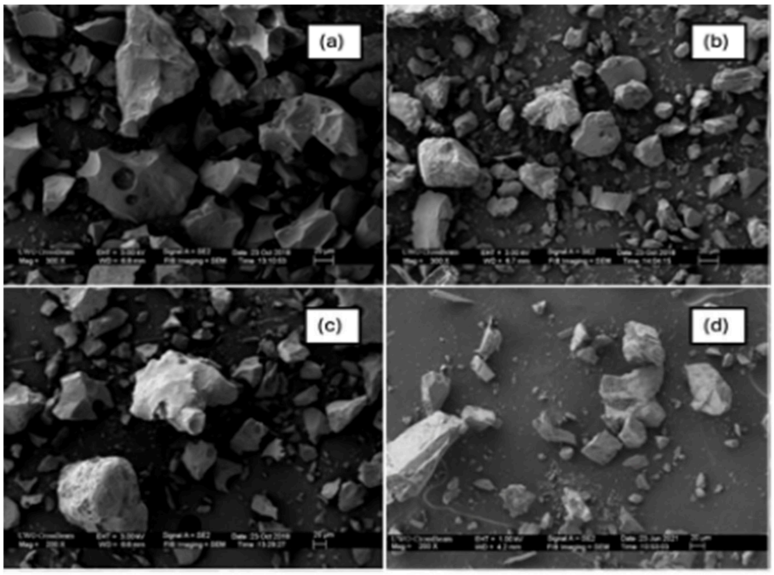


**Figure 3.** Lunar mare simulants: (**a**) CAS-1; (**b**) EAC-1; (**c**) OPRL2N; (**d**) LMS-1.

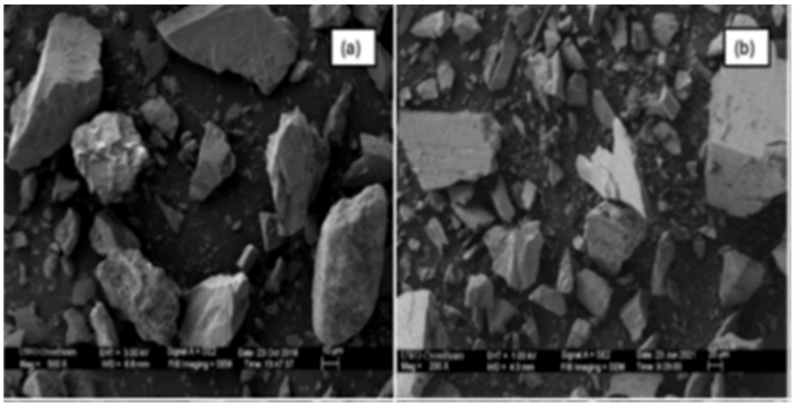


**Figure 4.** Lunar highland simulants: (**a**) OPRH2N; (**b**) LHS-1.

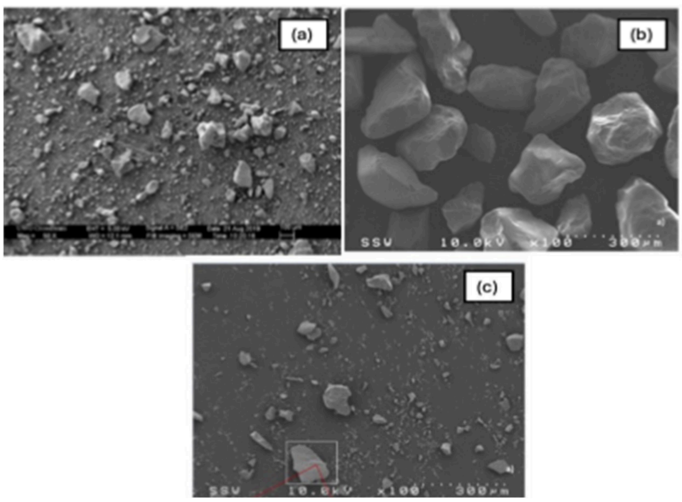


**Figure 5.** Martian simulant and benchmark terrestrial soils: (**a**) MMS-MG; (**b**) Toyoura sand; (**c**) silica flour (Sil-Co-Sil 106) [50].

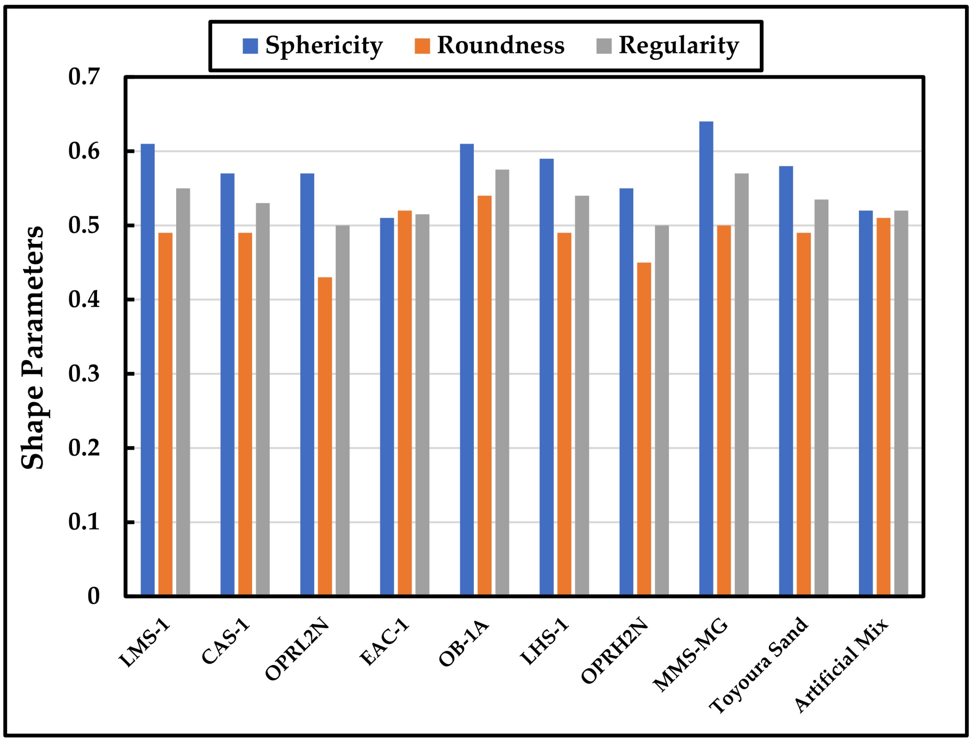


**Figure 6.** Particle shape parameters for all of the tested soils and simulants.

Although this was not attempted herein, it is interesting to note that [51] also found that the lunar regolith particle shapes for the two Apollo missions were quite similar and no significant shape differences were seen between small and large particles. In contrast, the shapes of the JSC-1A particles were quite different, with the aspect ratios being larger for smaller particles and smaller for larger particles. These observations likely show the influence of the different particle size reduction mechanisms: crushing for the simulant and meteorite impact for the lunar regolith. This suggests that size reduction via meteorite impact tends to preserve the shape, while crushing tends to increase particle non-sphericity as the particle size decreases. Ref. [52] discussed the intense mechanical abrasion that can occur through impact-induced particle motions, leading to more spherical regolith particles from originally fragmented/angular (impact) particles. Hence, regardless of maturity, the axial ratio (S) of lunar regolith becomes a trade-off between mechanical abrasion and impact fragmentation. In general, terrestrial soils have also been found to have similar particle shapes and mineralogies across all particle sizes, given that they often originate from similar sources and are deposited through similar geological processes [53]. Some materials can be found where the fines (silt) are from different sources compared to the coarser sand particles (e.g., [54]), resulting in different mineralogies and particle shapes within the same gradation. A few researchers (e.g., [55]) have also studied sands, silts, and their mixtures from single sources, resulting from identical mineralogies; some of these silts had different particle shapes because they were obtained by the natural crushing of coarser particles. With terrestrial soils, the particle shape is predominantly a function of the amount of physical weathering that occurs after removal (detachment) from the parent rock mass by erosive agents (e.g., water or wind) and is referred to as communition, which involves the mechanical breakdown, fragmentation, and modification/size reduction of the soil particles during transport and deposition.

It has been demonstrated that the particle shape influences the possible packing states of different soils [56]. The limit void ratio ($e_{max}$ and $e_{min}$) trendlines from a meta-study of natural terrestrial sandy soils with varying shapes (S and R) are shown in

Figures 7 and 8 [56], along with trendline confidence intervals based on ± one standard deviation from these data. Also plotted in these figures are the corresponding values from the current study for the lunar simulants and terrestrial soils. These plots show that both $e_{max}$ and $e_{min}$ (and the difference between them) increase with reductions in both S and R for the terrestrial soils. Thus, irregularity in particle shape appears to hinder particle mobility and the attainment of a dense packing configuration. In extreme cases, platey particles can even bridge gaps and create large open voids. It can also be seen that S and R for these natural soils show a wider range of values [S = 0.5 to 0.9 and R = 0.3 to 0.9], demonstrating the possible influence of variations in shape due to physical weathering. It should also be noted that these relationships are based on sandy soils with $C_u \leq 2.5$ and they thus have relatively narrow ranges of particle sizes.

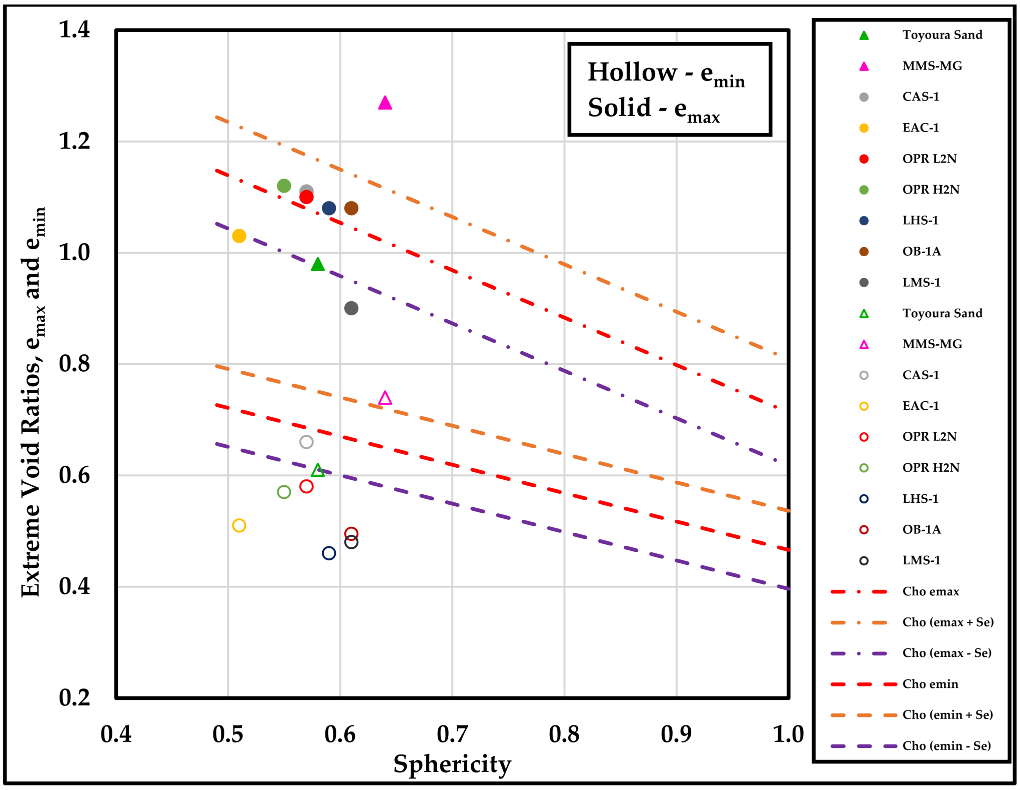


**Figure 7.** Effects of sphericity (S) on limit void ratios for terrestrial materials from [56] and simulants/soils from this study.

Comparison of the lunar simulants and the MMS-MG material in Figures 7 and 8 shows values of $e_{max}$ generally lying above the trend lines for both S and R and $e_{min}$ lying below the trend lines. In comparison, the natural Toyoura sand lies very close to the trend lines in both plots. This is to be expected, since the coefficient of uniformity ($C_u$) for Toyoura sand is 2.1—see Table 3. In general, $C_u$ is found to be larger than 2.5 (and up to 12.5) for all of the crushed simulant materials. The influence of $C_u$ in natural materials on these limit packing states and gradations was investigated in [57], which found that both $e_{max}$ and $e_{min}$ were reduced with increasing $C_u$ (up to 12), which is supported by the previous work in [58].

Ref. [56] also found that S and R for crushed materials fell with a much narrower range than those shown for the natural materials in Figures 7 and 8. Thus, it can be seen that the simulants generally follow the packing behavior of other granular materials, but with some variations due to their evolution from crushing. The particle shape, gradation, and packing states have been found to have a considerable influence on the mechanical responses of soils [47,57] through particle-level interactions, and the results in the following sections will be discussed in light of these findings.

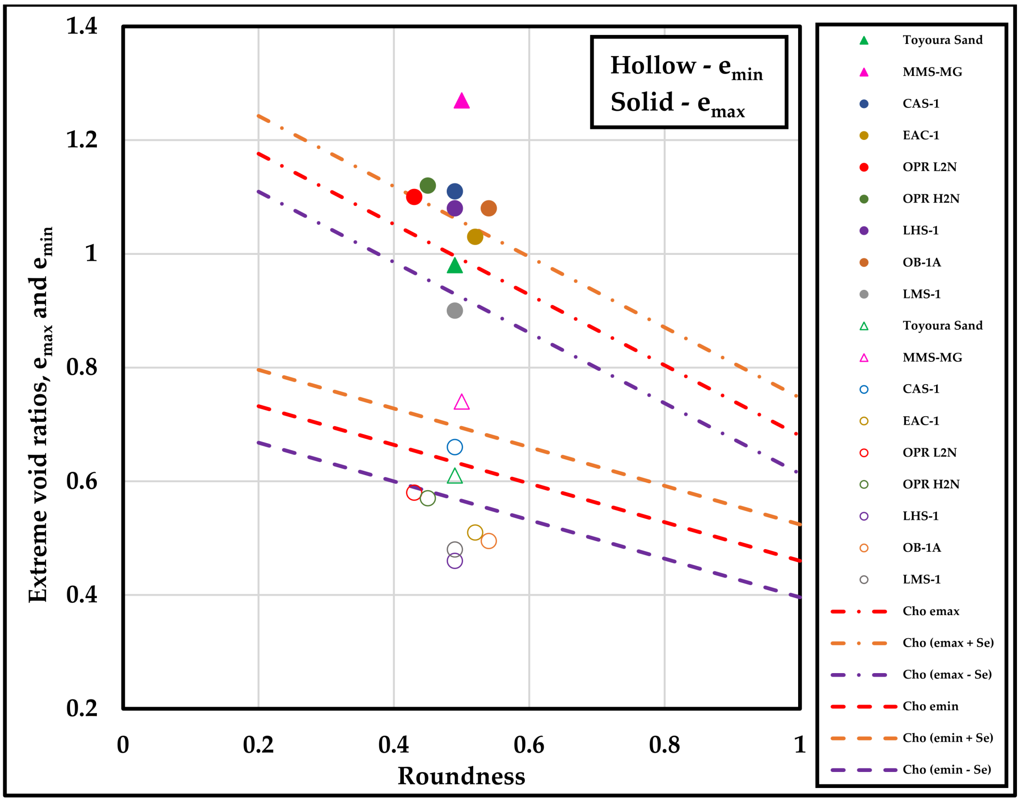


**Figure 8.** Effects of roundness (R) on limit void ratios for terrestrial materials from [56] and simulants/soils from this study.

### 3.3. Geomechanical Stress–Strain Tests

The oedometer test results derived from ASTM standard [45] for the simulant and soil samples at relative densities ($D_r$) of 30% and 60% are presented in Figures 9 and 10, respectively.

It is clear from Figures 9 and 10 that the initial void ratio ($e_{10}$—void ratio at 10 kPa, see Table 3) decreases with an increase in relative density for all materials. The void ratio (e) decreases non-linearly with an increase in vertical stress (loading condition) and then increases again with a decrease in vertical stress $\sigma_v$ (unloading condition) for all simulants. This behavior is consistent with the standard behavior of terrestrial soils. The slopes of these curves in relation to changes in vertical pressure can be characterized using the parameters $C_c$ and $C_r$ [for loading and unloading] according to

$$C_c \; or \; C_r = \frac{de}{dlog\,(\sigma_v)} \tag{4}$$

and can be used to describe the compressibility of materials under 1D [vertical] loading.

The simulants show generally similar compressibility (see Figure 11) and recompression behavior ($C_c$ and $C_r$), whose values are reduced for higher initial densities (i.e., from $D_r$ = 30 to 60%). These values are higher than those typically found for terrestrial soils [56], apart for Toyoura sand, and show the same reductions in compressibility with regularity ($R_g$) as found in [56]. The materials also show different $C_c/C_r$ ratios, from approximately 2 to 16 (see Table 3), with reductions at a higher relative density (60%). Although [56] observed that increased particle irregularity (and therefore lower S and R) leads to higher compressibility and decompression due to different packing densities and more particle contacts, this is only evident for the simulants at the higher relative density of 60% and is less clear at 30%.

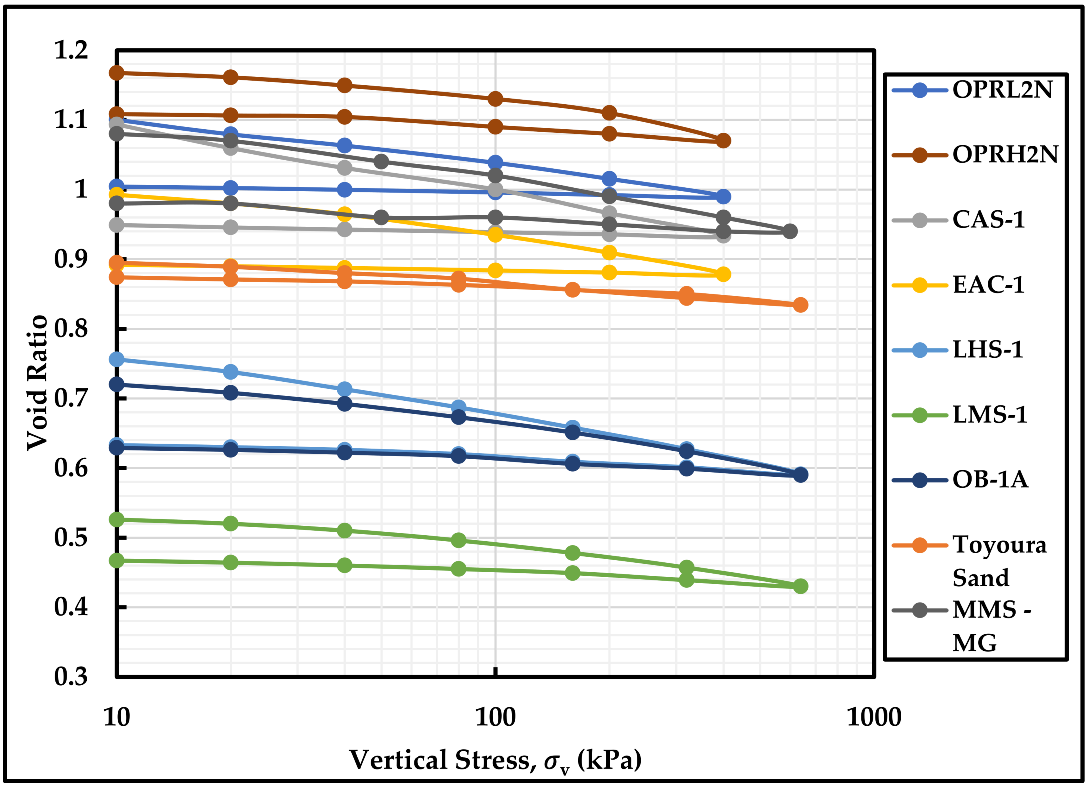


**Figure 9.** Lunar simulant and soil 1D compression results for loose packing states ($D_r$ = 30%).

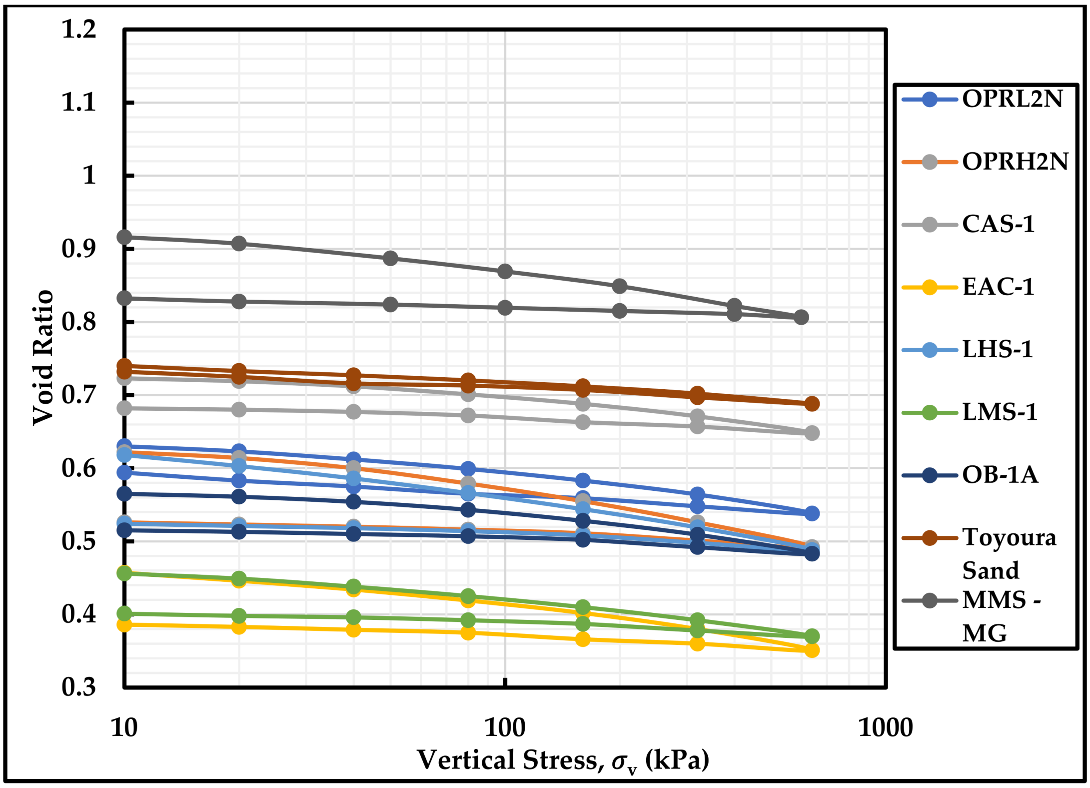


**Figure 10.** Lunar simulant and soil 1D compression results for dense packing states ($D_r$ = 60%).

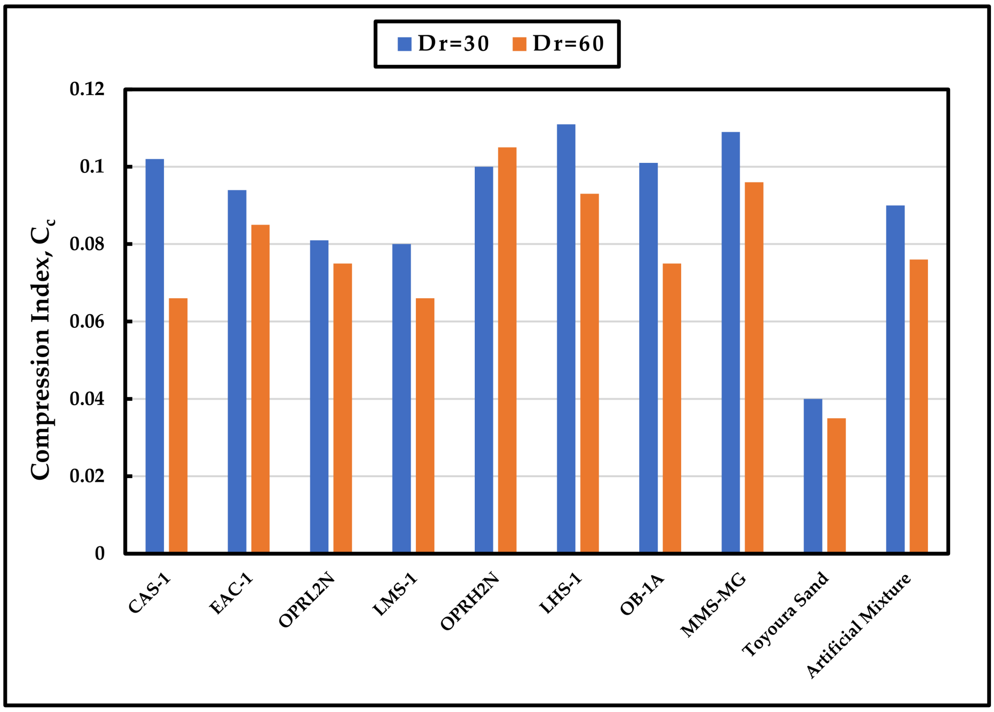


**Figure 11.** Compression indices of lunar simulants, Martian simulant, and terrestrial soils at $D_r$ = 30% and 60%.

Numerical studies of the influence of the particle shape in [59] for mono-sized grains under 1D loading found only minimal influences on compressibility and a greater influence on the yield stress, as well as differences in the development of $K_o$ [the ratio of horizontal to vertical stress], leading to higher horizontal stresses for angular particles. During unloading, more angular particles were found to retain higher horizontal stresses due to interlocking, and this also influenced the elastic unloading, with a lower Poisson's ratio (ν) and recompression indices, which was seen in the more irregularly shaped simulants (particularly at a 60% relative density). Ref. [60] suggested that lower $C_u$ values lead to higher compressibility ($C_c$) and more particle breakage (from fewer grain contacts), but this was not observed in the current data set. This may be due to the complex interplay between the particle shape (S and R), gradation ($C_u$), and particle size ($D_{50}$) among the simulants, making it difficult to isolate this effect.

Some typical direct shear test results are shown in Figures 12–15 for shear stress (τ) vs. horizontal displacement (dh) and vertical displacement (dv) vs. horizontal displacement. The data presented are for two of the simulant materials, EAC-1 and LHS-1, which bound the stress–strain responses of the various simulants and are therefore quite informative. Additional individual test results for the other simulants are discussed in greater detail elsewhere [17]. Although the $e_{max}$ value for both simulants is similar, the gap between the $e_{max}$ and $e_{min}$ limit void ratios is narrower for EAC-1, so, despite the same relative densities for each pair of tests ($D_r$ = 30 and 60%), the initial void ratios ($e_{10}$) are quite different. In terms of basic geotechnical characteristics, the two materials also show some significant differences: (i) the $C_u$ of LHS-1 (6.4) is smaller than that of EAC-1 (9), giving a narrower range of particles; (ii) the mean particle size of LHS-1 ($D_{50}$) is significantly larger at 0.1 mm compared to that of EAC-1 of 0.026 mm; and (iii) the shape parameters for LHS-1 (S = 0.59 and R = 0.49) show fewer angular particles than in EAC-1 (S = 0.51 and R = 0.52).

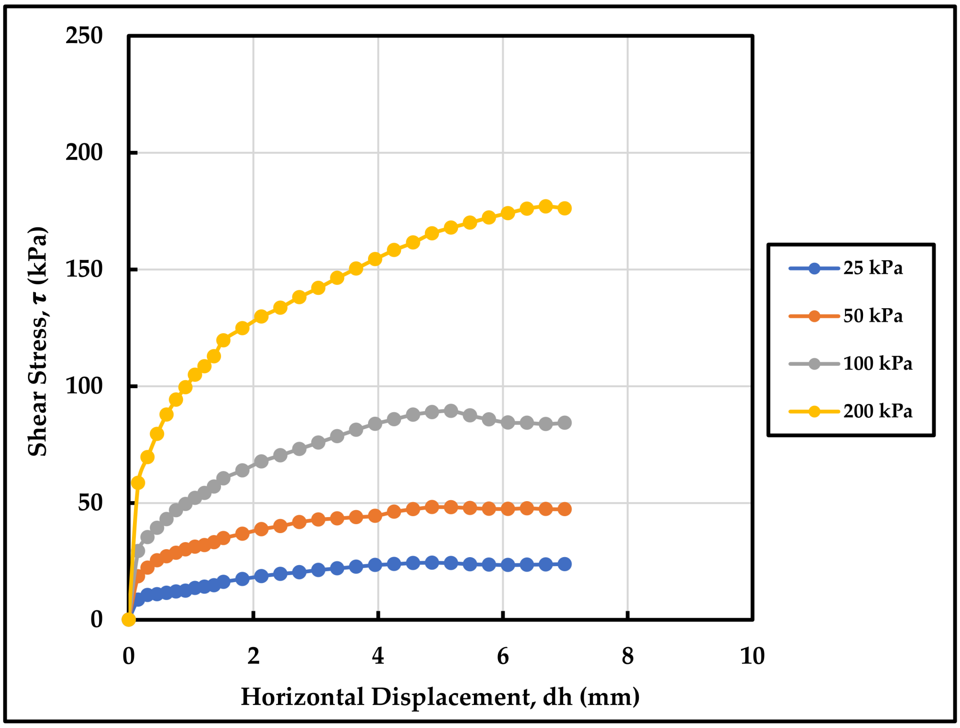


(**a**)

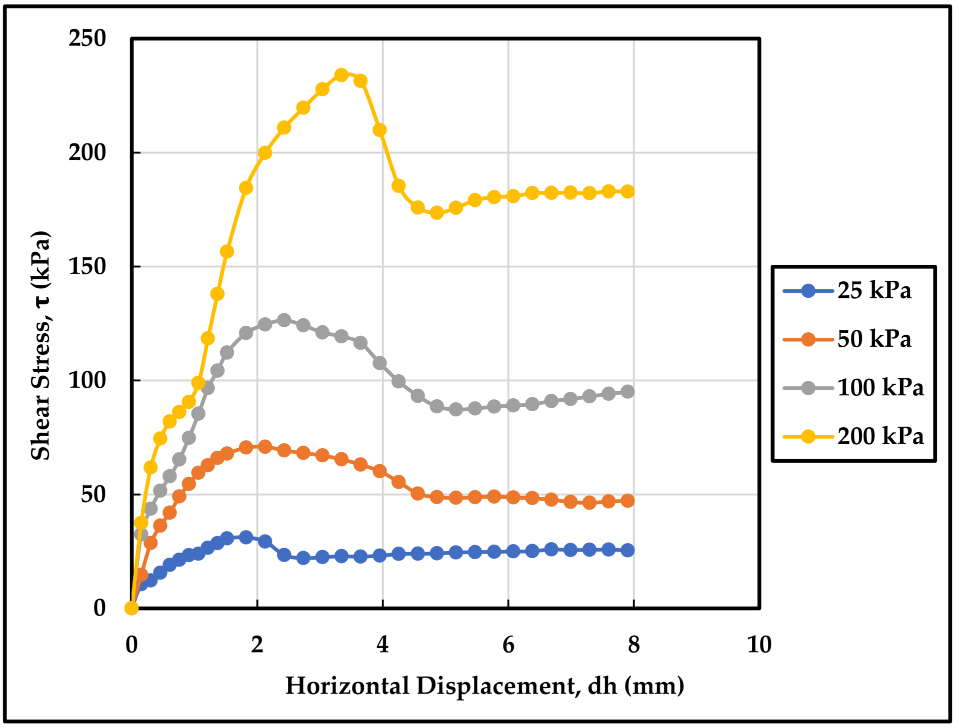


(**b**)

**Figure 12.** Direct shear, stress–strain: (**a**) EAC-1, Dr = 30%; (**b**) EAC-1, Dr = 60%.

The shear stress vs. horizontal displacement plots (for a range of normal or confining stresses $\sigma$ from 25 to 200 kPa) show typical responses for granular materials, with different relationships for the different relative densities [$D_r$ = 30% (loose) and 60% (medium dense)]. In general, increasing mobilized shear stresses (τ) are seen up to the peak values for higher confining stresses (σ) and relative densities. In addition, the form of the curve changes with the relative density; loose samples strain-harden to a peak at high horizontal displacements, whereas dense samples strain-harden to a peak more quickly and then strain-soften, with the final τ/σ value being similar to the equivalent displacement in the loose samples. These two points are usually referred to as the 'peak' and 'critical-state' (or post-peak) values. What is also noticeable in the graphs is that the peak and critical-state shear stress values are generally larger for EAC-1 than LHS-1 for equivalent normal stresses ($\sigma$) and relative densities ($D_r$).

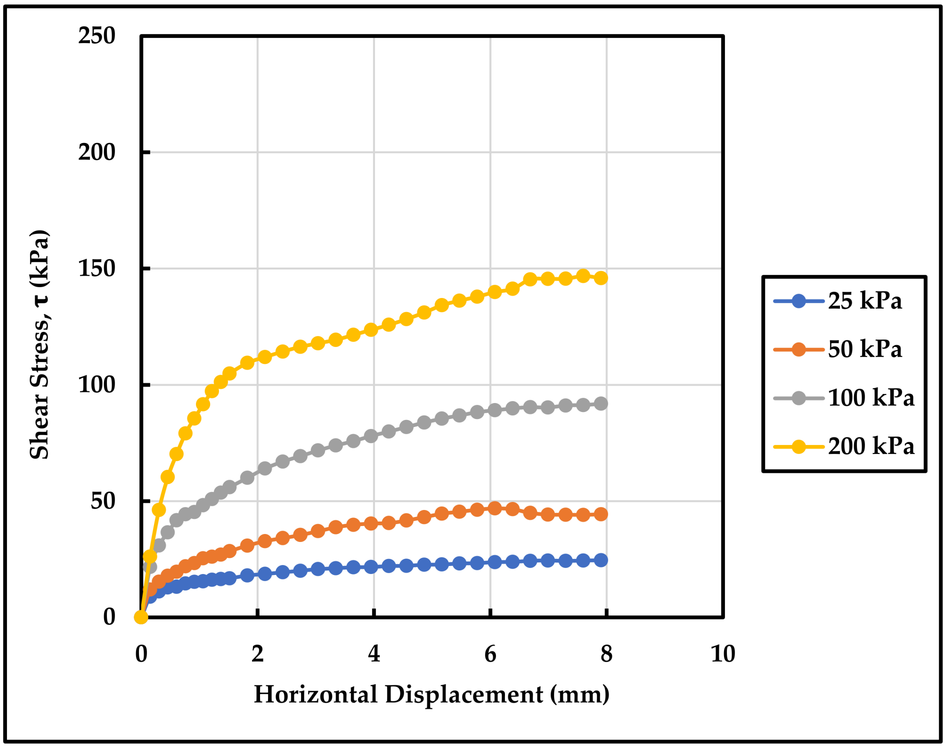


(**a**)

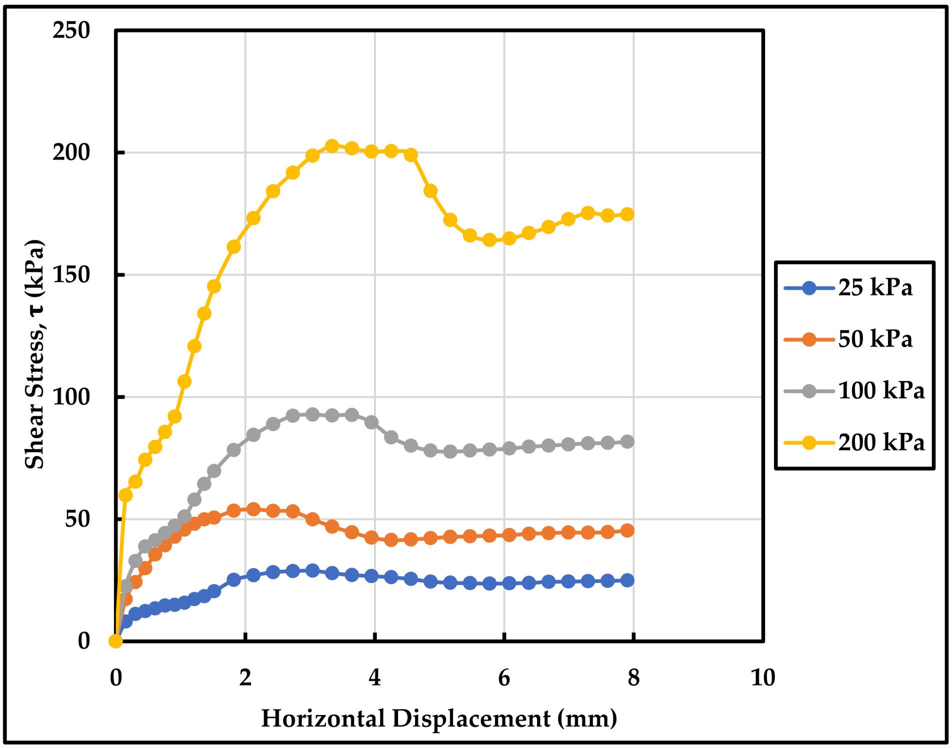


(**b**)

**Figure 13.** Direct shear, stress–strain: (**a**) LHS-1, Dr = 30%; (**b**) LHS-1, Dr = 60%.

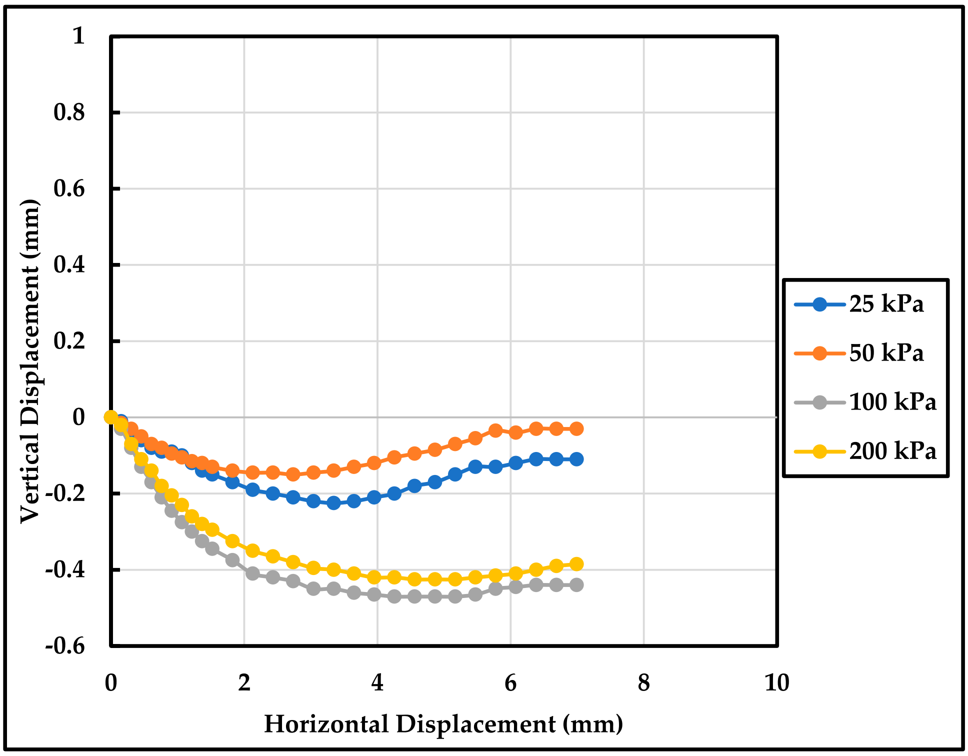


(**a**)

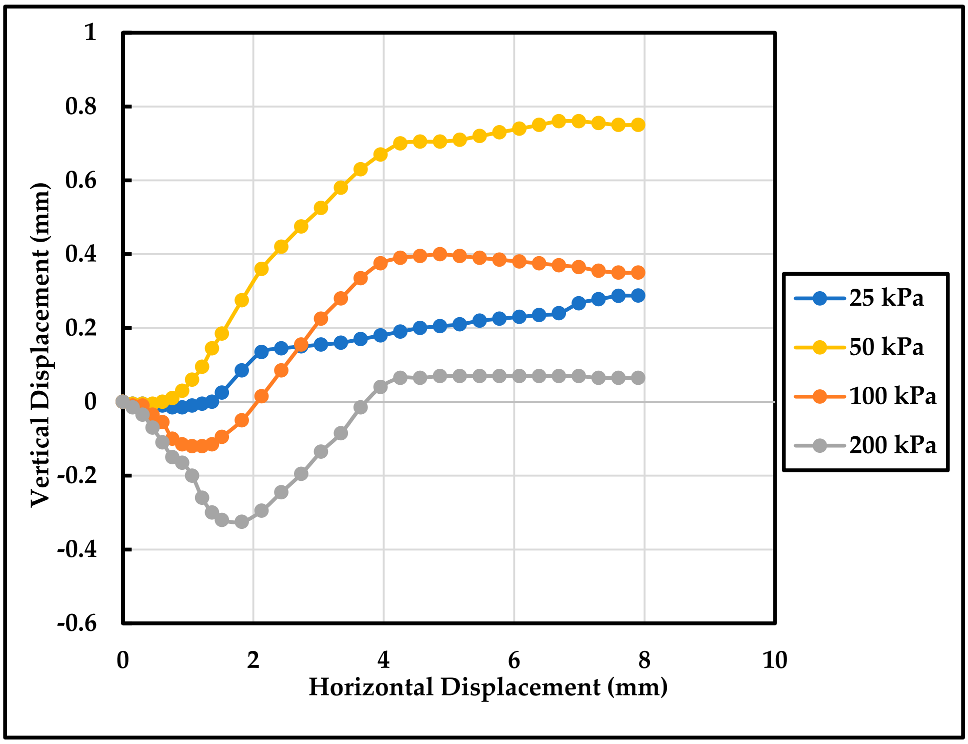


(**b**)

**Figure 14.** Direct shear, vertical displacement vs. horizontal displacement: (**a**) EAC-1, $D_r$ = 30%; (**b**) EAC-1, $D_r$ = 60%.

The companion graphs (Figures 14 and 15) for the same materials show the volumetric changes for the samples during the shearing process. The samples all compress initially (i.e., reduced volume, which is shown as negative vertical displacement, dv), with the loose samples continuing to do so and the dense samples then dilating (expanding in volume, with positive vertical displacement) for the remainder of the test. Also seen for both sets of samples at high strains is that the ratio of dv/dh is approximately 0 and thus the volume change towards the end of the test ceases. This is one definition of a 'critical state', where the soil is shearing as a frictional fluid with a constant volume [61]. Also noticeable is that, for the dense samples, the maximum dilation [i.e., the highest dv/dh] occurs at approximately the same horizontal displacement as the peak shear stress shown in Figures 13 and 14. The remainder of the simulant samples have responses that lie between these two extremes. Terrestrial soils (TS and AM) have similar general behavior but with lower peak values; the AM sample also has very low dilation responses.

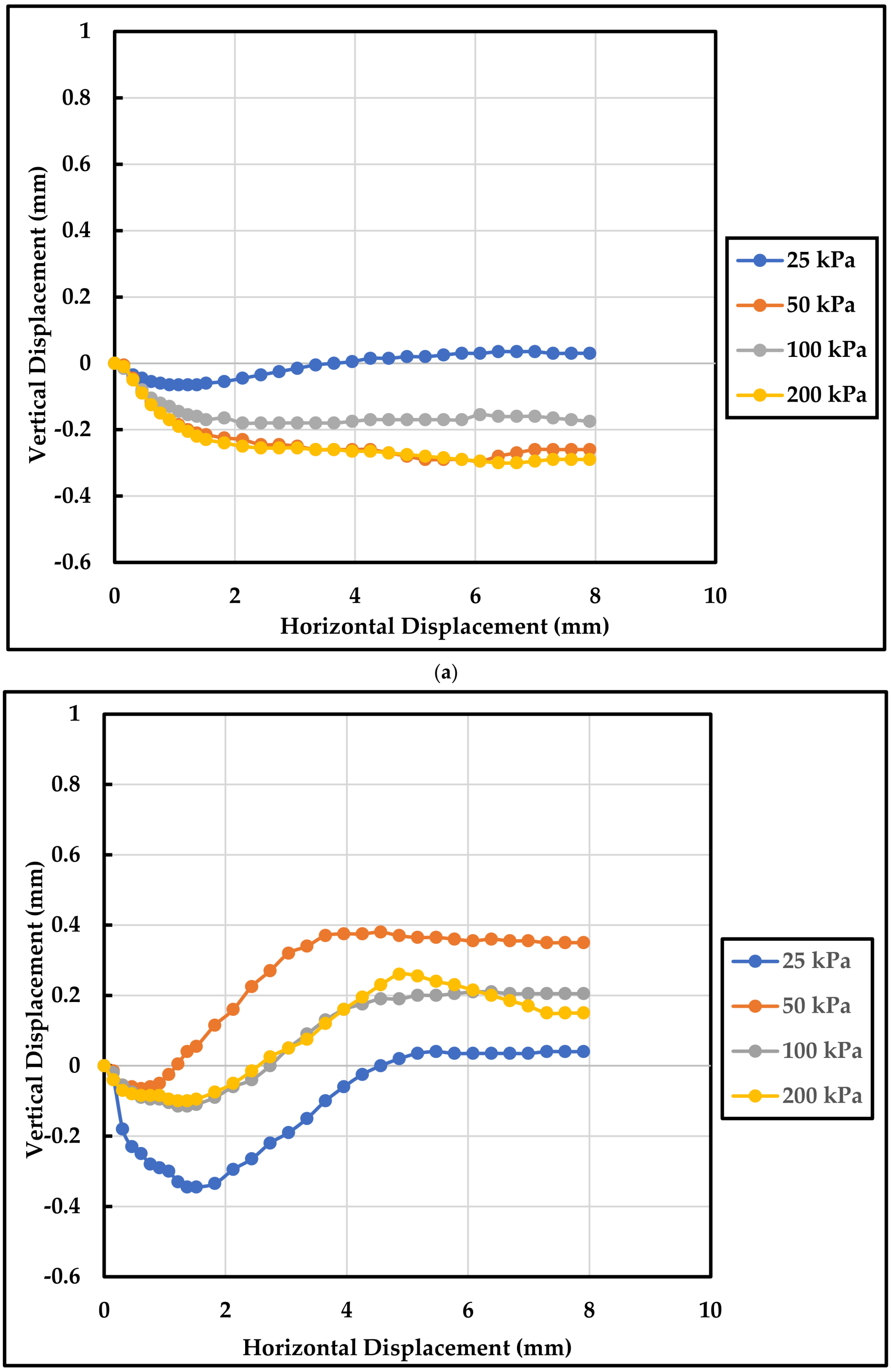


**Figure 15.** Direct shear, vertical displacement vs. horizontal displacement: (**a**) LHS-1, Dr = 30%; (**b**) LHS-1, Dr = 60%.

Granular soils develop shear resistance through two primary mechanisms: interparticle sliding friction and geometrical interference between particles [62,63]. Interparticle sliding friction occurs when adjacent particles slide along their contact surfaces and is represented by the interparticle friction angle ($\phi_\mu$). This friction angle depends mainly on the particle mineralogy and the roughness of the surface and is largely independent of the confining stress and density. Surface roughness is emergent from the strength, texture, and hardness of particles, which are governed by the structures of their constituent minerals [64]. The roughness features that control interparticle friction typically have smaller characteristic amplitudes than those associated with the particle angularity [65]. Reported values of $\phi_\mu$ for common minerals indicate ranges of approximately 22–35° for feldspar and 36–38° for quartz [64].

Geometrical interference, often referred to as particle interlocking, develops during shearing as particles thrust against, pass around, and sometimes damage neighboring particles. This mechanism is represented by a geometrical interference friction angle ($\phi_g$), whose magnitude varies with the effective confining pressure, ranging from about 0° at high confining pressures, where particle motion occurs primarily through sliding and particle damage, to approximately 30° at very low confining pressures, where movement involves particles colliding with or traversing adjacent grains. Geometrical interference can be further divided into two components: resistance due to dilation or particle overriding ($\phi_d$) and resistance associated with particle rearrangement and breakage ($\phi_p$) [64]. Accordingly, the mobilized friction angle during shearing can be expressed as

$$\phi_{mob} = \phi_\mu + \phi_p + \phi_d \tag{5}$$

The dilation component, $\phi_d$, depends on the initial density of the soil and the level of confining stress [66,67], as well as the particle surface roughness [68]. Dilation evolves throughout the shearing process, and the peak friction angle ($\phi_{pk}$) occurs when the dilation reaches its maximum. For example, Ref. [69] reported dilation angles approaching 30° for reconstituted sand tested under extremely low confining stresses (0.05–0.5 kPa). As the initial void ratio increases, the contribution of dilation decreases, and the geometrical interference component becomes dominated by particle rearrangement and damage.

At the critical void ratio defined in [70], dilation drops to zero. The friction angle corresponding to this condition is referred to as the constant-volume friction angle ($\phi_{cv}$) or the aforementioned critical-state friction angle ($\phi_{cs}$). Under constant-volume conditions, particle rearrangement and damage ($\phi_p$) can typically contribute an additional 5–6° to the mobilized friction angle [64].

Figures 16 and 17 show the Mohr–Coulomb failure envelopes from the direct shear box for the two simulants. We show the limit shear strength ($\tau_f$) by plotting shear stress ($\tau$) against normal stress ($\sigma$) for the multiple samples/confining stresses ($\sigma$) and fitting the well-known linear Mohr–Coulomb failure criterion to the data [71,72]:

$$\tau_f = c + \sigma.tan\phi \tag{6}$$

where the slope equals the friction angle ($\phi$), and the intercept is the cohesion (c).

These have been plotted for both the peak states and the critical states. By definition, the critical-state line passes through the origin (c = 0), with the slope representing the critical-state friction angle ($\phi_{cs}$), and therefore only peak cohesion values are presented herein (in Table 4).

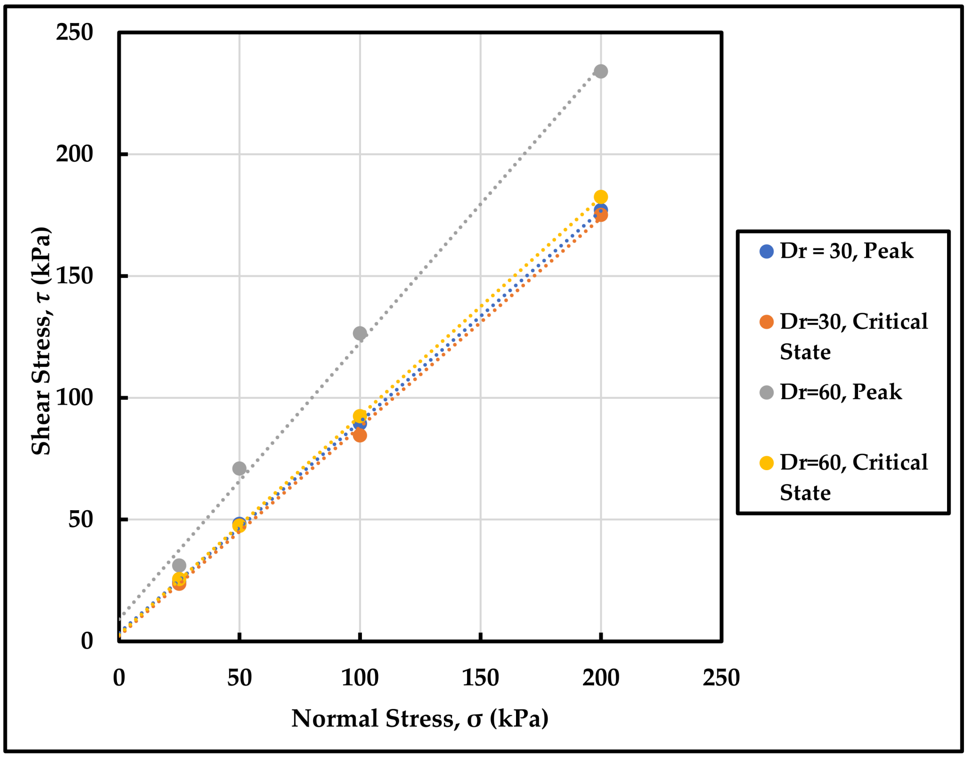


**Figure 16.** Direct shear: shear strength vs. normal stress (EAC-1).

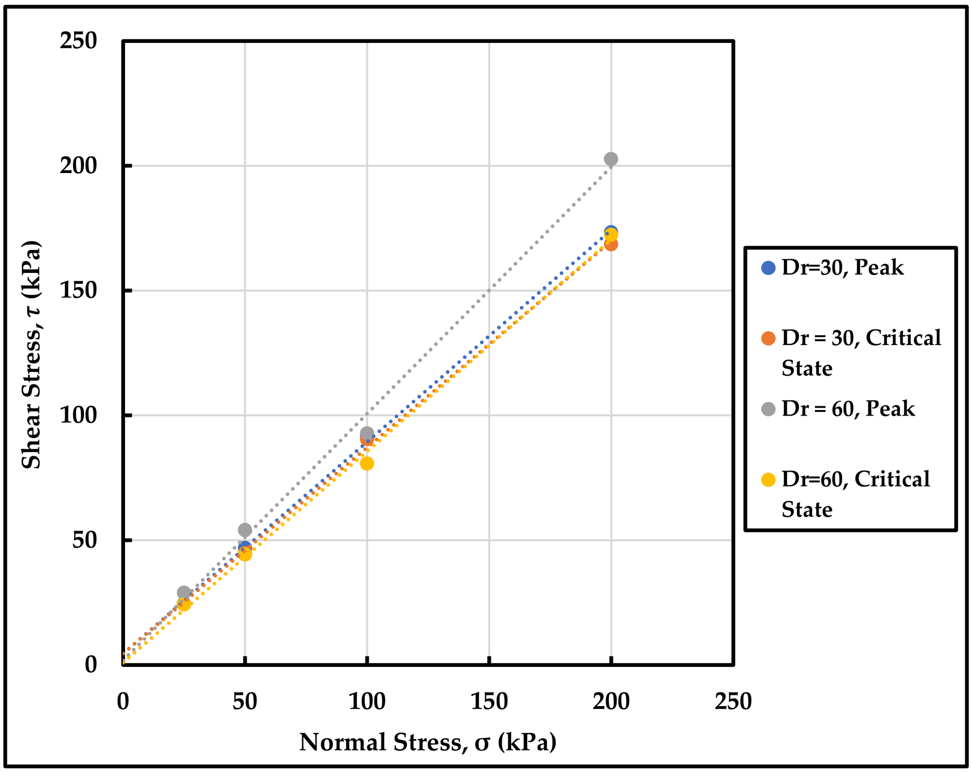


**Figure 17.** Direct shear: shear strength vs. normal stress (LHS-1).

The data in Figures 16 and 17 show very similar critical-state values for both relative densities and the peak line for the relative density of 30% (i.e., the loose state), whereas the peak lines for the two simulants are different. This manifests itself in different peak friction angles $\phi_{pk}$ of 48.6° and 44.6° for EAC-1 and LHS-1, respectively, and critical-state angles of approximately 40° to 41° ($\phi_{cs}$) for both materials. Since both simulants are predominantly plagioclase feldspar, this critical-state friction angle value falls within the expected range of $\phi_\mu$ plus 5° to 6°, and the difference between the critical-state friction angle value and the peak value is close to the variation in $\phi_d$ (difference between the slopes of the two M-C envelopes) for the two materials. This variation between the two materials is likely due to the particle size, $C_u$, and shape differences.

**Table 4.** Shear strength parameters of lunar simulants, Martian simulant, and terrestrial soils at different relative densities.

| Soil Type | $D_r$ | $Ø_{pk}$ | $\Delta\phi_{ex}$ | $c_{pk}$ | $\Psi_{-max}$ | α |
|---|---|---|---|---|---|---|
| EAC-1 | 30 | 41.1 | 8 | 3.5 | 13.6 | 0.59 |
| | 60 | 49.1 | | 9.1 | | |
| L2N | 30 | 40.4 | 10.9 | - | 18.2 | 0.60 |
| | 60 | 51.3 | | 13 | | |
| H2N | 30 | 38.8 | 6.5 | - | 8.6 | 0.76 |
| | 60 | 45.3 | | 3.4 | | |
| LHS-1 | 30 | 39.3 | 6.3 | 5 | 8.0 | 0.79 |
| | 60 | 45.6 | | 2 | | |
| CAS-1 | 30 | 41.4 | - | 13 | - | - |
| | 60 | - | | - | | |
| MMS-MG | 30 | 39.9 | 5.3 | 3.8 | 7.1 | 0.74 |
| | 60 | 45.2 | | 10 | | |
| Toyoura Sand | 30 | 31.5 | 5.2 | 0 | 6.3 | 0.82 |
| | 60 | 36.7 | | 2.5 | | |
| Artificial Mix | 30 | 34.2 | 2.6 | 1.2 | 4.3 | 0.60 |
| | 60 | 36.8 | | 7.5 | | |

The comparable data for the terrestrial soils (TS and AM) show critical-state friction angles of approximately 33° to 34°, which again fall within a reasonable range for quartz-based materials, with the additional variations being due to shape, gradation, and particle size differences. The higher friction angle values for the plagioclase feldspar materials compared to quartz are consistent with findings for other similar natural sands (e.g., Mississippi sand with 75% albite) using other forms of shear test [73]. High peak friction angle values have also been observed in tests on lunar regolith [4] from Apollo, i.e., 30° to 50°, and are consistent with those of plagioclase feldspar, olivine, and pyroxene and other silicate minerals found in the lunar crust [74,75]. The difference between the peak and critical-state friction angles ($\phi_{pk}$-$\phi_s$) is known as the excess friction angle ($\Delta\phi_{ex}$) [76]. This stress–dilatancy relationship can be represented using

$$\Delta\Phi_{ex} = \alpha.\, \Psi_{max} \tag{7}$$

where α is a coefficient. This coefficient was found to be approximately α = 0.48 and 0.8 for triaxial compression and plane strain, respectively, in [77] for clean quartz sands, and it is a function of the intermediate principal stress ratio (b). Further investigation in [78] showed that α was also a function of the gradation ($C_u$) and reduces with increasing $C_u$. The authors also found that there was a weak dependence on the critical-state friction angle ($\phi_{cs}$), with increases in α for lower friction angles. Table 4 shows a range of values of α from 0.59 to 0.82 for the simulants ($\Psi_{max}$), which fall into the range found in [78] and follow similar dependencies on the gradation and critical-state friction angle. The peak cohesion ($c_{pk}$) and friction angles ($\phi_{pk}$), peak dilation angles, excess friction angles ($\Delta\phi_{ex}$), and stress–dilatancy coefficients ($\alpha$) for all tested materials are presented in Table 4.

There are different approaches to determining the critical-state friction angle ($\phi_{cs}$), which rely on interpreting single or group tests. The direct measurement of the friction angle, mobilized to large strains at which the dilation rate is zero (critical state), is shown in Figures 16 and 17 (based on the data in Figures 12 and 13), and the results are presented in Table 4. Another method using data, namely from multiple tests, involves the use of energy correction [79] and the sum of the stress ratio and dilation ($\xi = \tau/\sigma + dv/dh$), which is plotted against the shear displacement (dh). The plots in Figures 18 and 19 show the shear box data presented in this manner for the EAC-1 and LHS-1 materials, respectively. The data for all tests (for different confining stresses and relative densities) collapse onto a constant value of $\xi$, which is assumed to be $\xi = \tan\phi'_{cs}$. This gives a range of $\phi'_{cs}$ of 40–44° and 38–44° for EAC-1 and LHS-1, respectively, supporting the findings of the other method used. Similar analyses have been performed on benchmark round quartz sands in [80], on Leighton Buzzard sand ($\phi_{cs}$ = 29.9°), and on Ottawa sand ($\phi_{cs}$ = 26.1°) [79], as well as angular crushed limestone [81], with $\phi_{cs}$ = 36–40°, showing the influence of both the mineralogy and particle shape on the estimations. A similar match was found for the TS and AM soils tested in this study. The study in [56] determined $\phi_{cs}$ = 42°—17R for quartz sands, and this seems to be a significant underestimation for the lunar simulants, which are better represented by $\phi_{cs}$ = 45.7°—9.5S. It should be noted that the former relationship also applies to low-$C_u$ (<2.5) materials, and the low-$C_u$ materials (H2N) have been removed from this expression fit; therefore, it only applies to well-graded materials with $C_u$ > 6.

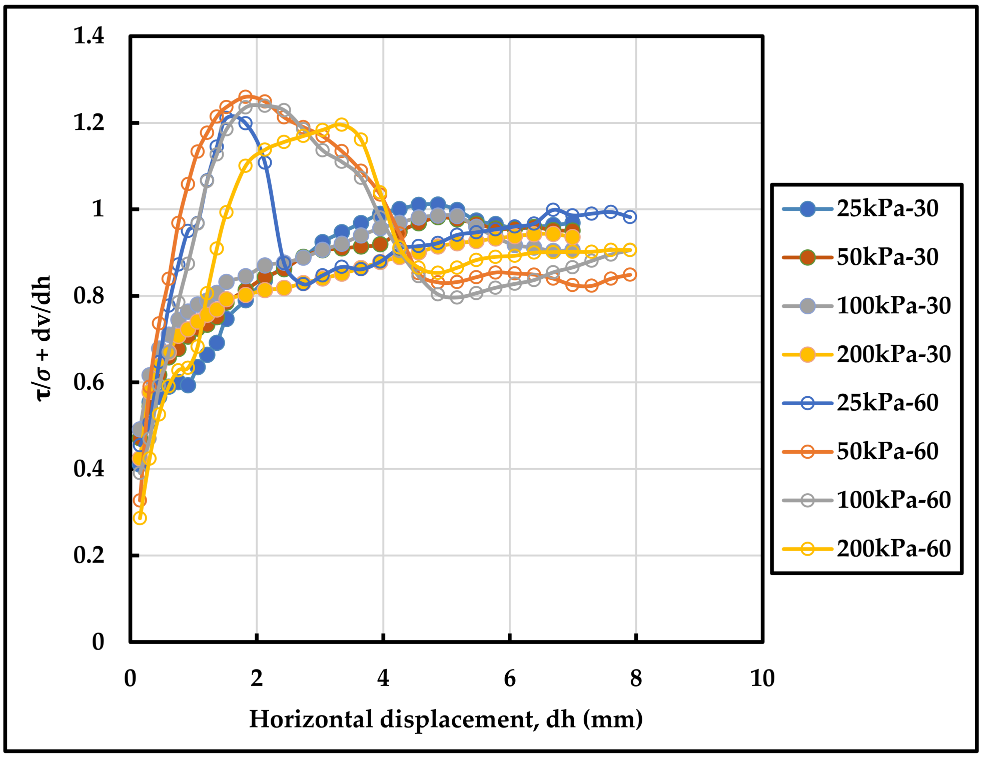


**Figure 18.** Sum of stress ratio and dilation against horizontal displacement for EAC-1 at $D_r$ = 30% and $D_r$ = 60%.

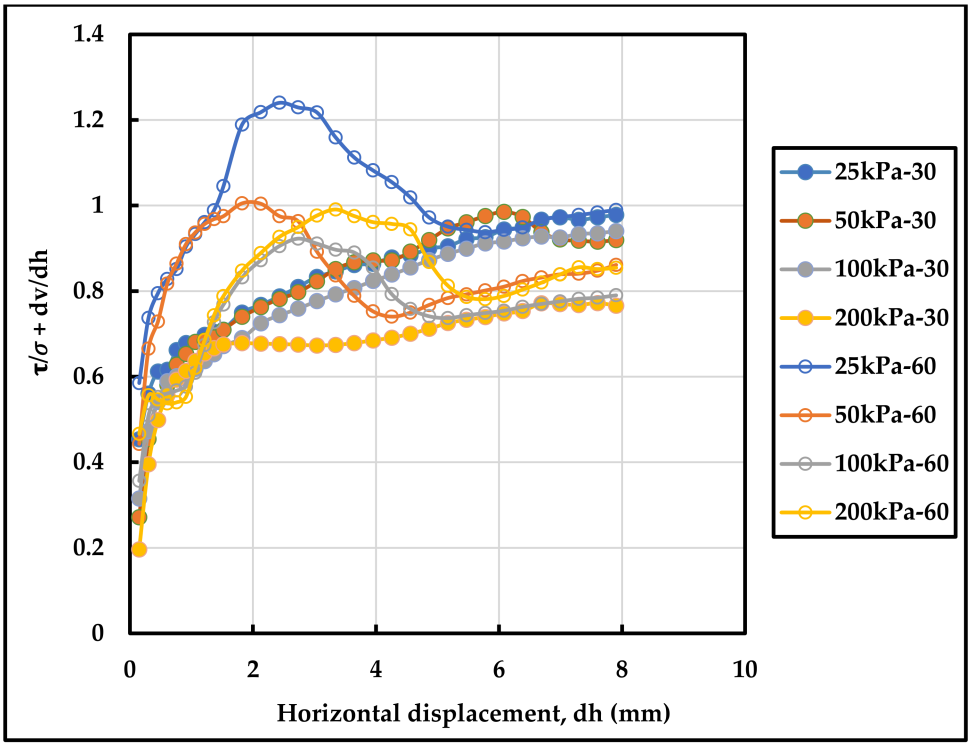


**Figure 19.** Sum of stress ratio and dilation against horizontal displacement for LHS-1 at Dr = 30% and Dr = 60%.

Figure 20a shows the peak dilation angles ($\Psi_{max}$) for the different materials at a range of confining pressures (σ) for $D_r$ = 60%. This demonstrates the different dilatory responses for the various materials and the influence of the minerology, particle size and distribution, and particle shape. If a similar plot were constructed for the $D_r$ = 30% case, the dilation angles would be proportionately smaller, showing the significant influence of the relative density. Also noticeable is the reduction in dilation with increasing pressure (known as pressure suppression), which is due to the additional energy required for particle/asperity ride-up, leading to higher rates of asperity damage and breakage and, consequently, reduced dilation. Both of these influences on the dilation angle have been reported previously (e.g., [82]), and the average maximum dilation angle over this stress range is shown in Table 4. Also demonstrated by other researchers (e.g., [57]) is a reduction in dilation as the gradation changes (i.e., $C_u$ decreases). This behavior is captured by the relationship below (after [77]):

$$A_{\Psi}.I_R = \alpha.\Psi_{max} \quad (8)$$

where $A_{\Psi}$ = 3 for triaxial conditions and 5 for plane strain. $I_R$ is known as the relative dilatancy index and is given by

$$I_R = D_r.[Q - \ln(p')] - 1 \quad (9)$$

where Q is a fitting parameter related to mineral hardness, and p′ is the mean normal stress (=[$\sigma'_1 + 2\sigma'_3$]/3).

Q was originally proposed to have a value of 10 for quartz sands with low $C_u$ [77] and was later refined to cover a range of 7 to 11 by different researchers (e.g., [83]). The data in Figure 20a have been replotted in Figure 20b as the normalized dilation angle ($\Psi_{max}/\Psi_{max\text{–}200}$) against the mean normal stress (p). The value of $\Psi_{max}$ at 200 kPa has been used for normalization, since further increases in stress have very little influence on the dilation. The mean normal stress was found by calculating the earth pressure coefficient $K_o$ for the different materials.

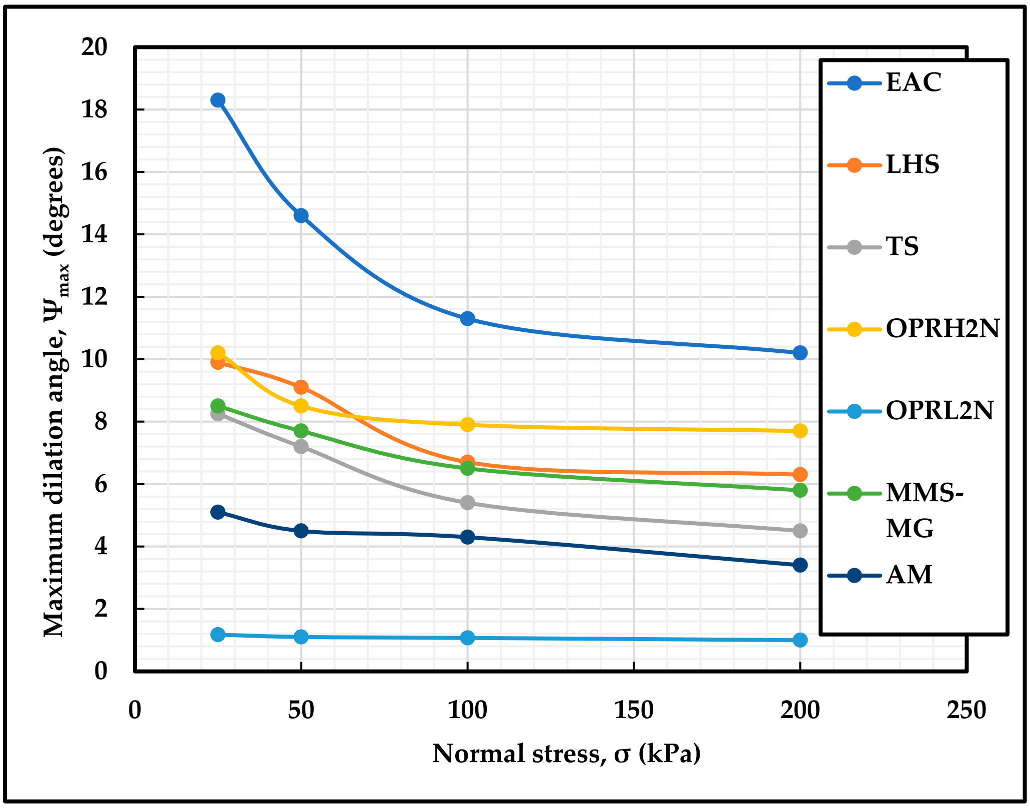


(**a**)

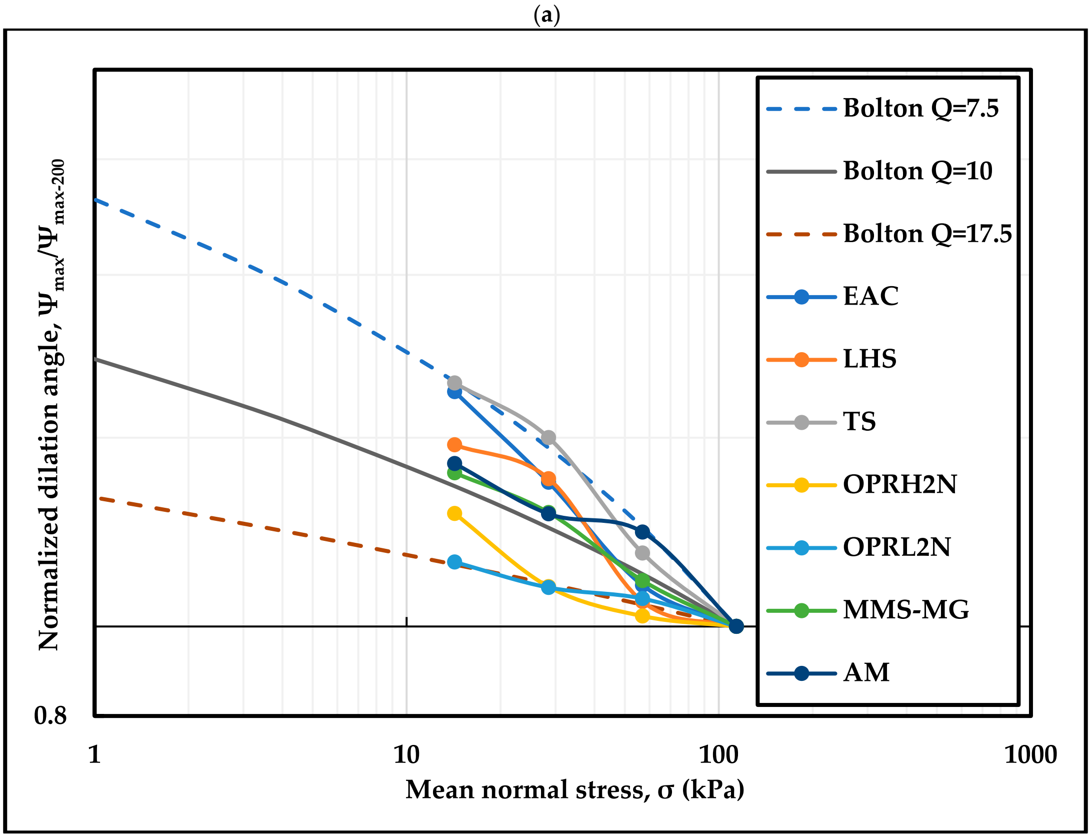


(**b**)

**Figure 20.** (**a**) Maximum dilation angle vs. normal stress for Dr = 60% for various samples. (**b**) Normalized maximum dilation angle vs. mean normal stress.

Also plotted are the curves obtained using the equation in [77] at the appropriate $D_r$, with three values of Q: 7.5, 10, and 17.5. These are seen to bound the lunar simulants and the terrestrial soils, with the original estimate of 10 from [77] lying close to the average. The value of Q = 7.5 fits the Toyoura sand (TS) curve, which is similar to that reported in [83] with Q = 8.4. These lines have been extrapolated back to much lower stresses ($p$ = 1 kPa or σ = 1.75 kPa), which is not possible in a standard direct shear device, and provide angles of dilation of the order of 30–38°, which is in the same range as found in [69] for very low stresses. This suggests that this type of approach may be helpful to estimate very low stress friction angles for various scenarios.

## 4. Discussion

Future construction on the Moon will require specialized geotechnical approaches for a range of construction and mining projects. Of particular importance is to ensure the stability of foundations and slopes under conditions that can differ significantly from those on Earth. Lunar infrastructure, such as habitats, storage facilities, landing pads, radiation shields, and transportation routes, will interact directly with the lunar surface (regolith), which consists of fragmented rock, dust, and breccia produced by meteorite impacts [84,85]. Since this material is in a distinctive environment with unique mechanical properties, traditional Earth-based geotechnical design methods are likely to need adaptation [86]. The strength and stiffness properties of such granular materials are emergent from the interactions of the individual particles and dependent on the self-weight stresses of the material. Thus, a major challenge is the Moon's low gravity, which alters the vertical stress distribution within the regolith [87], thereby affecting the foundation bearing capacity, settlement behavior, and slope stability. Additionally, the absence of an atmosphere and extreme temperature variations can affect the long-term mechanical behavior of the regolith and structural materials; repeated thermal cycling may alter particle contacts and lead to gradual changes in regolith strength or stiffness, degrading structural performance. Geotechnical investigations, including in situ testing, sampling, and the use of lunar soil simulants on Earth, are therefore essential to help estimate regolith properties and develop reliable design parameters [88]. By integrating geotechnical engineering principles with environmental constraints, lunar engineers can ensure stable geotechnical structures for the safety and functionality of future lunar communities.

### 4.1. Findings from Current Study

Since direct in situ geotechnical lunar regolith measurements are sparce and limited largely to sampling, trenching observations and simple surface interaction experiments were conducted during the Apollo program [4]. The density and porosity vary quite significantly, both vertically and laterally, across the lunar surface. The upper 0–10 cm 'fluffy' layer has low relative densities ρ = 1.3–1.5 g/cc ($D_r$ = 25–50%), with void ratios lying in the range of e = 1.8–0.8 (porosities, $n$ = 0.65–0.45), compared to the underlying dense layers (ρ = 1.6–1.9 g/cc) with a high relative density ($D_r$ = 65–100%) and void ratios in the range of e = ~0.65 ($n$ = 0.4). This variation is due to rearrangement and loosening from the ongoing lunar micrometeorite flux, and the dense and consolidated lower layer has been more tightly packed over lunar geological time and may also have experienced seismic and other impact vibrations [89]. Due to the lack of available lunar materials, engineers rely heavily on terrestrial simulants to understand the mechanical behavior of regolith across this range of states. These simulants are engineered to approximate the particle size distribution, angularity, mineralogy, and bulk density of lunar regolith, thereby enabling laboratory measurements of stress–strain responses and geotechnical parameters for use in analytical and numerical stability models.

https://doi.org/10.3390/aerospace13060527

The current study has compared the mechanical behavior of a range of commonly available lunar simulants and three benchmark terrestrial soils with varying properties. Toyoura sand was chosen since it is a very well-characterized material and is composed primarily of quartz with a significant percentage of alkali feldspar. It is also known to be more angular than typical terrestrial natural sands. The artificial mixture added a (1:2 by volume) percentage of ground silt-sized quartz to the Toyoura sand and thereby increased the coefficient of uniformity ($C_u$) from a low value (2.1) to an intermediate value (3.9). Finally, MMS-MG is a plagioclase crushed rock with a high $C_u$ of 10 (>6 indicates well-graded), which is similar to the higher simulant values. The grains are also relatively angular. The terrestrial soils' grains have specific gravity ($G_s$) of approximately 2.65, and, although some of the simulants have similar values, the average is closer to that of lunar regolith, with a value of 2.9. The simulants have a wide range of average particle sizes ($D_{50}$), from 26 to 100 μm (with an average for the seven simulants of 72 μm), which compares to lunar regolith, with a $D_{50}$ of approximately 70 μm, and the terrestrial materials are generally coarser by three to four times. Finally, the sphericity and roughness (S and R) of the simulants and terrestrial soils span a similar range and are comparable to those of lunar regolith. Thus, these soils are believed to span the ranges of geometric and material characteristics of the simulants and therefore provide reasonable points of reference to assess the influences of the grain size, shape, mineralogy, and grain size distribution on the mechanical responses of the various materials.

The comparison of $\rho_{max}$, $\rho_{min}$, $e_{10}$ ($D_r$ = 30%), $C_c$, $C_r$, $\phi_{pk}$, and $c_{pk}$ in Tables 3 and 4 generally shows similar values to those of lunar regolith (1.9, 1.1, 1.07, 0.1–0.11, $C_c$/10, 41 to 50°, and 0.1–5.9 kPa; [48]) for both the lunar simulants and the terrestrial soils. The results also demonstrate the importance of the mineralogy, particle shape, average particle size, coefficient of uniformity, and relative density to the mechanical responses of the materials, with MMS-MG being the closest of the terrestrial soils to the simulants. Also apparent is the influence of crushing preparation on the mechanical responses of these materials. While the mode of fracturing is likely different for the different mineralogies (conchoidal for the quartz and glasses, leading to crescent/lobe/wedge shapes; cleavage for the pyroxene and plagioclase, leading to rectangular prisms), few differences in S and R were discernable within the artificially created simulants measured herein. Likewise, it is feasible that the modes of fracture may be different for different testing rates, and this has not been assessed in this study. The high critical-state and peak friction angles of the simulants are only matched by the response of MMS-MG, which shows the importance of the grain mineralogy, with the predominantly quartz soils mobilizing much lower critical-state values (but achieving similar dilation responses, which appear to be more influenced by the particle shape). Thus, the results from this study suggest that the judicious choice of a more widely available natural plagioclase feldspar silty sand (e.g., [73,90]), with suitable steps taken to remove the clay fraction (e.g., sedimentation or chemical amendments), might be feasible for a benchmark material and will provide much larger supplies for the laboratory testing of lunar construction. In addition, the invariance of these materials and lunar regolith with regard to the critical-state friction angle ($\phi_{cs}$) suggests that future stress–strain investigations can concentrate on identifying the dilatory responses over a range of pressures (with standard testing equipment), and extrapolation to very low stresses applicable to lunar conditions can be conducted with confidence to estimate the peak friction angle ($\phi_{pk}$).

### *4.2. Application to Slope Stability*

Slope stability is a critical concern for construction activities such as excavation, berm formation, embankments, regolith-based shielding systems, and the stability of natural slopes. Lunar regolith exhibits high peak and critical-state friction angles [91], and, due to a lack of natural cementation or moisture, this can result in different failure behaviors compared with terrestrial soils. Excavation slopes near habitats, underground storage areas, or transportation corridors must therefore be carefully designed to prevent collapse, especially in regions with steep crater walls or accumulated loose regolith.

The reduced lunar gravity will influence both the driving and resisting forces within slopes. Lower gravity decreases the self-weight of the regolith, reducing downslope shear stresses. However, it simultaneously reduces normal stresses, which mobilize frictional resistance along potential (or existing) failure surfaces. In slope stability analyses, appropriate soil data can be incorporated into limit equilibrium methods [92], such as the method of slices, or into finite/discrete element numerical models [93] to assess low-gravity responses. Sensitivity analyses of terrestrial slopes consistently demonstrate that friction angle selection exerts a stronger influence on the predicted stability than other geotechnical parameters for granular soils. As a result, the accurate characterization of the stress-dependent friction behavior of simulants, especially at low confining pressures, is critical for reliable design. This reduced-stress environment also significantly affects the dilation behavior, particle rearrangement, and potential strain localization, which will ultimately influence the mobilized friction angle.

Knowledge of the peak, critical-state, and dilation angles and cohesion derived from simulant testing at representative confining stress levels for lunar conditions is paramount [21]. However, since the regolith thickness, density, particle size distribution, and degree of compaction will vary significantly across the lunar surface, spatial variability in strength parameters can also present challenges [94]. Since the factor of safety for a frictional slope is highly sensitive to the assumed friction angle, even small variations of a few degrees can significantly alter the predicted stability, particularly for slopes approaching the angle of repose. Accordingly, conservative lower-bound friction angles (i.e., $\phi_{cs}$) are often adopted in preliminary analyses, supplemented by parametric studies to bound possible stability outcomes. Although shear strength parameters obtained from the laboratory testing of lunar soil simulants will provide reasonable estimates of the friction angles and cohesion values, because in situ data from the Moon are limited, initial design approaches will likely incorporate quite conservative assumptions and higher safety factors. As more lunar exploration missions collect geotechnical and structural performance data, these models can be refined to improve their accuracy.

### *4.3. Application to Foundation Design and Construction*

For foundations, both the ultimate and serviceability limit states are investigated during design, namely the bearing capacity and the settlement [95]. Accordingly, the peak friction angle is the dominant strength parameter in classical bearing capacity theory. For shallow foundations, the ultimate bearing resistance is expressed as a function of the unit weight, foundation width and embedment, and bearing capacity factors that depend exponentially on the friction angle [96]. Even small variations in the assumed angle of the order of a few degrees can produce large changes in the calculated bearing capacity factors, such as $N_q$ and $N_\gamma$, leading to substantial differences in predicted allowable loads.

While reduced lunar gravity can increase the theoretical bearing capacity of shallow foundations, it may also reduce confining stresses in the soil mass, potentially decreasing the shear strength and influencing failure mechanisms. This is accommodated for in terrestrial soils (with low relative densities) by using reduced bearing capacity factors (e.g., [97]), but this atypical combination of high friction angles and low confining pressures on the Moon may also lead to progressive failure [98] and produce a situation whereby the majority of the slip surfaces in the failure mechanism only mobilize the much lower critical-state angle of friction ($\phi_{cs}$), thereby reducing the foundation loading capacity. Accurate assessment of these effects is therefore essential for designing safe and efficient foundations for lunar structures.

In common with the slope stability problem, the friction angle of lunar regolith is a fundamental parameter in estimating the bearing capacity of foundations intended for lunar infrastructure. Because direct geotechnical data from the Moon are limited, engineers must rely heavily on terrestrial simulants to characterize the mechanical behavior. Laboratory testing of these materials should therefore provide reasonable estimates of the peak and critical-state friction angles, which will form the basis for preliminary foundation design. Reduced gravity directly affects the unit weight term in bearing capacity equations and indirectly influences stress distribution beneath foundations. While lower gravity reduces driving stress, it also limits confinement, which may affect the mobilized shear strength. In addition, laboratory tests conducted under Earth atmospheric conditions do not replicate the lunar vacuum environment [99]. The absence of moisture and the presence of electrostatic forces on the Moon may influence particle contacts and the apparent frictional resistance. These environmental differences introduce uncertainty in extrapolating laboratory-derived friction angles to in situ conditions.

To manage these uncertainties, designers should employ parametric analyses using a range of plausible friction angles obtained from simulant testing. Both the ultimate and allowable bearing capacities should be evaluated for shallow footings supporting habitats, landing pads, and support towers. Sensitivity studies show that bearing capacity predictions are highly responsive to the assumed friction angle, often more so than to variations in foundation geometry or embedment depth. Consequently, conservative lower-bound friction angles should be adopted for preliminary design, with factors of safety reflecting the limited in situ validation.

One-dimensional (1D) oedometer compression testing of lunar regolith simulants provides a primary basis for estimating foundation settlement [100] on the Moon. Because in situ compressibility data are extremely limited, terrestrial simulants are again necessary to characterize the settlement response of regolith under controlled laboratory conditions. In a 1D oedometer test, a laterally confined specimen is subjected to incremental vertical loading, enabling the determination of the constrained modulus, compression index, and stress-dependent stiffness parameters. Under low confining stresses representative of shallow lunar foundations, compression behavior will be governed by particle rearrangement and crushing at contact points, and, as seen in this study, oedometer-derived modulus values are therefore quite sensitive to the relative density [93]. Care is usually taken to determine the pre-consolidation pressure of soils (the previously experienced maximum confining pressure) to enable the choice of the compression index ($C_c$) or recompression index ($C_r$) in settlement calculations. However, this threshold of pressure is currently unknown for lunar regolith [4] and, given the particularly low values of $C_c$, may not necessarily be important in foundation design. Settlement analyses typically integrate the constrained modulus over the anticipated stress increase beneath a foundation, assuming an elastic or nonlinear stress–strain response. Parametric evaluation using upper- and lower-bound modulus values is common to address uncertainty in simulant representativeness and environmental differences. Thus, oedometer data provide a practical framework for the preliminary prediction of the immediate settlement of lunar surface foundations.

The last part of this section provides an example of a foundation bearing capacity analysis using some of the laboratory data found during this study and discusses some of the implications. The bearing calculations given below are based on a circular foundation (with diameter B = 2 m), assumed to be sitting on the lunar surface. The ultimate bearing pressure ($q_f$) of a centrically, vertically loaded foundation (ignoring any cohesion of the regolith or embedment of the foundation) can be found using the classical bearing capacity Equation (10) [96]:

$$q_f = ½\, s_\gamma.\gamma.B.N\gamma \quad (10)$$

where B is the foundation width (m), $\gamma$ is the soil unit weight (kN/m$^3$), $s_\gamma$ is the shape factor (=0.6 for a circular foundation), and $N_\gamma$ the self-weight bearing capacity factor.

If we ignore the upper 10–15 cm of the vertical lunar regolith profile, then a reasonable average density ($\gamma$) over the zone of influence of the foundation (3B/2) is 1.8 g/cc. The self-weight bearing capacity factor ($N_\gamma$) is a function of the mobilized friction angle along the various shear surfaces of the failure mechanism underneath the foundation. The simplest approaches would be to take (i) the range of peak friction angles found ($\phi_{pk}$ = 45 to 50°) or (ii) the critical-state friction angle ($\phi_{cs}$ = 40°) for the simulants. Classical bearing capacity factor ($N_\gamma$) charts/tables are often limited to the upper friction angle (50°), and $N_\gamma$ is known to be more difficult to estimate for higher angles. For these three different friction angle values, the associated $N_\gamma$ values [96] are, respectively, 109.4, 270.8, and 762.9. With the given unit weight under lunar gravity, the ultimate bearing capacities are therefore 192.9, 479.4, and 1345.7 kPa, respectively. Option (i) is standard practice for terrestrial foundations, but it should be noted that these $N_\gamma$ values are calculated using 'associated' plasticity theory and thus assume a dilation angle equal to the friction angle ($\psi_{max}$ = $\phi_{pk}$). There has been much discussion in the geotechnical literature (e.g., [101]) as to whether there is a physical limit to the amount of dilation that can occur for granular materials, and these values of $N_\gamma$ may therefore not be physically realistic, even for low stresses and high material relative densities.

Option (ii) may represent the limit of a phenomenon known as 'progressive failure' [98,102]. Classical foundation theories assume that failure occurs simultaneously along the failure mechanism slip surfaces beneath a foundation. In reality, failure is progressive since plastic strains in soil are highly non-uniform, preventing the uniform mobilization of shear strength across the mechanism. Traditional assumptions that soil strength parameters remain constant under large strains may be inadequate, especially for strain-softening soils like dense sands under low stresses. Instead, localized zones of intense shear strain, known as shear bands, form first. Within these zones, the strength quickly decreases from the peak to critical state as the strain increases. Stress redistribution then drives the propagation of shear bands, gradually forming a less complete slip-surface mechanism. At failure, the mobilized strength will then lie between the peak and critical-state values. Taking the fully reduced friction angle may be overly conservative, and other approaches that reduce $N_\gamma$ by 15–30% may be more reasonable (e.g., [103]), properly capturing the reduction in the mobilized dilation angle with strain. Thus, the $N_g$ value for a friction angle of 50° would be reduced to 534 and the associated ultimate bearing capacity would be 942 kPa.

The preceding calculations provide the 'capacity' of the system, and, in the absence of a 'demand', it is common practice for allowable bearing pressures ($q_a$) to be limited to 100–300 kPa for foundations bearing dense silty sand materials based on settlement and factor-of-safety criteria. If this value is modified for lunar conditions, then allowable bearing pressures of 35–50 kPa would be deemed appropriate. Hence, the majority of factors of safety (F = $q_f/q_a$) would be well in excess of those in standard terrestrial practice of 2–3, although these values will drop quite significantly as the friction angle approaches 40°. This exercise is quite informative since it illustrates several aspects of both the material and foundation behavior (and standard geotechnical practice). Firstly, the material behavior (in terms of the friction angle and mobilized dilation angle) and our foundation analysis approaches appear to be at the limits of our current knowledge. Secondly, we do not have experience of loading foundations in scenarios where the material is dense (and will likely significantly strain-soften following peak strengths being reached), but the associated stress field (from regolith self-weight and the foundation loading) is very small. The phenomenon of 'progressive failure' may therefore need to be more adequately investigated, and subsequent analytical approaches may need to be developed for lunar foundation systems.

### 4.4. Choice and Application of Stress–Strain Tests

Experimental research studies of lunar simulants have predominantly concentrated on direct shear (a plane-strain test) for determining stress–strain and strength behavior. Terrestrial geotechnical engineering generally recognizes the need for the use of a range of strength tests (for different conditions) and often favors the triaxial compression test [104] due to its better control of stress conditions and reduced limitations regarding the enforcement of shear bands in the samples [105]. In addition, the triaxial test is much better suited to axi-symmetrical problems (such as foundations), whereas plane-strain testing (particularly the simple shear test) is more applicable to long structures such as slopes and embankments. Thus, there is currently a gap in the literature, where a range of varying relative densities and confining stresses have been employed with the testing of simulants under triaxial test conditions. Although peak friction angles for lunar regolith [4,91] have been reported to range between about 35° and 50°, with higher values observed for dense specimens and at low confining stresses, the different shearing modes in these two tests also mean that the friction angles will be 2–5° lower for triaxial measurements due to constraints on the intermediate principal stress, and dense materials are also found to dilate less in plane-strain testing. Hence, care must be taken to apply the correct test in any geotechnical application when preparing for lunar construction. Thus, the application of simulant-derived friction angles to lunar design calculations will likely require several modifications to conventional terrestrial approaches. In addition, theoretical relationships exist to convert between plane-strain and axi-symmetrical-derived friction angles (e.g., [106]), but these should be confirmed to provide robust estimates for lunar regolith and simulants given the different mineralogies involved.

Applicable stress ranges for various tests also need to be determined since standard terrestrial testing is usually constrained to low confining pressures of 15–20 kPa. Most of the previous testing that has been reported in the literature has concentrated on stress ranges that span in situ stresses and have not accounted for stress changes due to lunar construction. For instance, in the above bearing capacity example, below a foundation, the vertical extent of the underlying bearing capacity failure surface is usually assumed to be 3B/2 (i.e., one and a half times the foundation diameter). The in situ vertical stress average from the lunar surface below the 2 m foundation to the edge of the mechanism will be approximately 4.5 kPa (assuming $\rho = 1.8$ g/cc). If we invoke terrestrial foundation practice, then the allowable bearing pressures should be less than 300 kPa in dense silty sands, and the modification of this for lunar gravity leads to a surface pressure (q) not exceeding 50 kPa. Applying elastic half space theory [107] at the midpoint of this zone of influence below the foundation, the change in pressure will be between 20 and 50% of the surface pressure (q); thus, the stress experienced by this material will be in the range of 15–30 kPa and falls within the abilities of typical terrestrial equipment.

### 4.5. Summary

Finally, the continued refinement of simulant formulations, laboratory-based shear testing and soil mechanics interpretation, geotechnical design and construction, and future robotic and crewed site investigations will be required to reduce the uncertainty with regard to the development of lunar construction. This will also be driven by the transition from national government-based exploration and exploitation to private industry and the development of a lunar construction practice with experienced consultants and contractors.

## 5. Conclusions

This study has systematically evaluated the mechanical behavior of a suite of commonly used lunar simulants and compared them with three benchmark terrestrial soils that were selected to span a representative range of mineralogical, granulometric, and morphological characteristics. The terrestrial materials—Toyoura sand, an artificial quartz–silt mixture, and MMS-MG—were shown to provide a useful framework for isolating the influence of the particle size distribution, grain shape, and mineralogy on the soil response. In particular, the selected materials capture a broad range of coefficients of uniformity, particle angularity, and grading, enabling a meaningful comparison with lunar regolith and simulants. The principal conclusions of the study are as follows:

- The specific gravity values of the simulants ($G_s$) approach those of lunar regolith and exceed those of typical terrestrial soils. This similarity is attributed to the incorporation of high-density constituents such as basaltic fragments, anorthosite, feldspar, and glass phases, which are representative of lunar surface mineralogy.
- The particle size distributions of the investigated lunar simulants generally fall within the established envelope of lunar regolith reported from Apollo datasets. Despite variability in gradation, all simulants are classified as silty sand (SM) under the Unified Soil Classification System. The mean particle size ($D_{50}$) is broadly consistent with that of lunar regolith, although certain simulants exhibit relatively fine grading.
- Most simulants displayed lower coefficients of uniformity ($C_u$) than lunar regolith, likely reflecting the controlled mechanical crushing processes used in their production, which yield narrower gradations compared to the naturally well-graded regolith. However, the coefficients of curvature ($C_z$) were comparable to those reported for lunar soils. Further studies of wider size distributions more representative of lunar regoliths could be valuable to assess the influence on mechanical responses, particularly with respect to future construction activities.
- Quantitative image analysis indicates that simulant particles exhibit sphericity (S) and roundness (R) comparable to lunar regolith. Nevertheless, fundamental differences due to the formation processes are evident. Since lunar regolith's particle morphology is governed by impact comminution, and simulants are produced via mechanical crushing, there are distinct influences on the packing behavior, with irregular particle shapes reducing particle mobility and therefore altering the fabric.
- The measured limit void ratios ($e_{max}$ and $e_{min}$) of the simulants are lower than those inferred for lunar regolith but remain consistent with those of terrestrial granular soils. These parameters are governed by the particle shape, gradation, and fines content.
- Index and compressibility parameters ($e_{10}$, $C_c$, and $C_r$), as well as strength parameters ($\Psi_{pk}$ and $c_{pk}$), were found to align well with published lunar regolith ranges, reinforcing the validity of the use of simulants for geotechnical applications. The results also highlight that the mineralogy, particle angularity, gradation, and relative density exert first-order controls on the resulting mechanical behavior.
- Among the terrestrial soils, MMS-MG, which is a well-graded, angular, plagioclase-rich crushed rock, most closely replicates the strength characteristics of the lunar simulants, particularly in terms of the peak and critical-state friction angles. In contrast, the quartz-dominated materials exhibit lower critical-state friction angles, despite achieving comparable dilatancy, suggesting that the particle shape primarily governs the volumetric response, whereas the mineralogy plays a more dominant role in the transient (peak) shear strength.

- Importantly, the observed consistency in the critical-state friction angle across the simulants and lunar regolith indicates that future investigations may benefit from focusing on characterizing the dilatancy over a range of confining pressures with conventional laboratory equipment tests. Such data can then be reliably extrapolated to the low-stress conditions relevant to lunar environments to estimate peak strength parameters.
- These findings highlight the importance of carefully selecting and characterizing simulants to ensure fidelity in reproducing the mechanical response of lunar regolith for engineering applications on the Moon e.g., [108]. In addition, the study suggests that naturally occurring terrestrial plagioclase feldspar silty sands (suitably amended to remove the clay fraction) may serve as practical and scalable benchmark materials for lunar geotechnical and construction research, offering a viable alternative to limited and costly simulants. Although a plagioclase-rich basalt, crushed to a fine particle size, may prove to be more cost-effective, care should be taken regarding the time of crushing, since longer periods have been found to create more rounded shapes.

**Author Contributions:** Conceptualization, T.N. and G.R.O.; Methodology, T.N. and D.J.; Software, D.J.; Validation, D.J., T.N. and G.R.O.; Formal Analysis, D.J.; Investigation, D.J.; Resources, T.N. and G.R.O.; Data Curation, T.N. and D.J.; Writing—Original Draft Preparation, D.J.; Writing—Review and Editing, T.N. and G.R.O.; Visualization, T.N. and G.R.O.; Supervision, T.N. and G.R.O.; Project Administration, T.N.; Funding Acquisition, T.N. All authors have read and agreed to the published version of the manuscript.

**Funding:** This research was funded by the Natural Sciences and Engineering Research Council, grant number RGPIN-2015-06062.

**Data Availability Statement:** The raw data supporting the conclusions of this article will be made available by the authors on request.

**Acknowledgments:** The authors would like to acknowledge the technical support and help of both Aly Ahmed, Geotechnical Research Centre (UWO), and Xiao Chen Zhang, Earth Sciences (UWO), during the laboratory testing and SEM phases of the work.

**Conflicts of Interest:** The authors declare no conflicts of interest. The funding sponsors had no role in the design of the study; in the collection, analyses, or interpretation of the data; in the writing of the manuscript; or in the decision to publish the results.

## References

1. Kereszturi, A. Polar Ice on the Moon. In *Encyclopedia of Lunar Science*; Springer: Berlin/Heidelberg, Germany, 2023; pp. 971–980. [CrossRef]
2. Benaroya, H. Lunar habitats: A brief overview of issues and concepts. *REACH* **2017**, *7–8*, 14–33. [CrossRef]
3. Adachi, M.; Goda, R.; Naoya, H. Effects of particle size on the magnetic cleaning system for manned lunar explorations. *Acta Astronaut.* **2024**, *226*, 23–30. [CrossRef]
4. Connolly, J.; Carrier, W.D. An Engineering Guide to Lunar Geotechnical Properties. In *Proceedings of the 2023 IEEE Aerospace Conference, Big Sky, MT, USA, 4–11 March 2023*; IEEE: Piscataway, NJ, USA, 2023; pp. 1–9. [CrossRef]
5. Carrier, W.D. *The Four Things You Need to Know About the Geotechnical Properties of Lunar Soil*; Lunar Geotechnical Institute: Lakeland, FL, USA, 2005.
6. Nunn, C.; Pike, W.T.; Standley, I.M.; Calcutt, S.B.; Kedar, S.; Panning, M.P. Standing on Apollo's Shoulders: A Microseismometer for the Moon. *Planet. Sci. J.* **2021**, *2*, 36. [CrossRef]
7. McKay, D.S.; Blacic, J.D. *Workshop on Production and Uses of Simulated Lunar Materials*; LPI/TP-91-01; Lunar and Planetary Institute: Houston, TX, USA, 1991.
8. Weiblen, P.; Gordon, K. Characteristics of a Simulant for Lunar Surface Materials. In Proceedings of the Symposium on Lunar Bases and Space Activities of the 21st Century, Houston, TX, USA, 5–7 April 1988.
9. Sibille, L.; Carpenter, P.; Schlagheck, R.; French, R. *Lunar Regolith Simulant Materials: Recommendations for Standardization, Production, and Usage*; NASA/TP-2006-214605; NASA: Springfield, VA, USA, 2006.

10. Papike, J.; Taylor, L.; Simon, S. Lunar Materials. In *Lunar Sourcebook: A User's Guide to the Moon*; Heiken, G., Vaniman, D., Eds.; Cambridge University Press: Cambridge, UK, 1991; pp. 121–182.
11. Battler, M.; Spray, J. The Shawmere anorthosite and OB-1 as lunar highland regolith simulants. *Planet. Space Sci.* **2009**, *57*, 2128–2131. [CrossRef]
12. Nash, V.; Cowley, A.; Fateri, M.; Coene, S.; Siarov, S.; Cristoforetti, S. Human exploration initiatives at EAC: Spaceship EAC and the development of large-volume lunar regolith simulant for LUNA. In Proceedings of the European Planetary Science Congress, Riga, Latvia, 17–22 September 2017.
13. Manick, K.; Gill, S.-J.; Najorka, J.; Smith, C.; Duvet, L. Fundamental properties characterization of lunar regolith simulants at European Space Agency (ESA) sample analogue curation facility. In Proceedings of the 49th Lunar and Planetary Science Conference, The Woodlands, TX, USA, 19–23 March 2018.
14. Nieke, P.; Kita, J.; Haming, M.; Moos, R. Manufacturing Dense Thick Films of Lunar Regolith Simulant EAC-1 at Room Temperature. *Materials* **2019**, *12*, 487. [CrossRef]
15. Engelschion, V.; Eriksson, S.; Cowley, A.; Fateri, M.; Meurisse, A.; Küppers, U.; Sperl, M. EAC-1A: A novel large-volume lunar regolith simulant. *Sci. Rep.* **2020**, *10*, 5473. [CrossRef] [PubMed]
16. Newson, T.; Ahmed, A.; Joshi, D.; Zhang, X.; Osinski, G. Assessment of the Geomechanical Properties of Lunar Simulant Soils. In *Earth and Space 2021: Space Exploration, Utilization, Engineering, and Construction in Extreme Environments*; Susante, P., Roberts, A., Eds.; ASCE: Reston, VA, USA, 2021.
17. Joshi, D. Assessment of Geo-Mechanical Properties of Lunar Simulants. Master's Thesis, University of Western Ontario, London, ON, Canada, 2022.
18. Prabu, T.; Muthukkumaran, K.; Venugopal, I.; Anbazhagan, S. Assessment of shear strength and compressibility characteristics of a newly developed lunar highland soil simulant (LSS-ISAC-1) for Chandrayaan lander and rover missions. *Planet. Space Sci.* **2021**, *209*, 105354. [CrossRef]
19. Agarwal, A.K.; Kuo, Y.L.; Jaksa, M.B.; Scott, B.T. Density, strength and compressibility characteristics of lunar regolith simulant. In Proceedings of the Conference on Geomechanics, Cairns, Australia, 2–5 July 2023.
20. Long-Fox, J.; Landsman, Z.; Easter, P.; Millwater, C.; Britt, D. Geomechanical properties of lunar simulants LHS-1 and LMS-1. *Adv. Space Res.* **2023**, *71*, 5400–5412. [CrossRef]
21. Dotson, B.; Valencia, D.S.; Millwater, C.; Easter, P.; Long-Fox, J.; Britt, D.; Metzger, P. Cohesion and shear strength of compacted lunar and Martian regolith simulants. *Icarus* **2024**, *411*, 115943. [CrossRef]
22. Wroth, C.; Bassett, R. A Stress–Strain Relationship for the Shearing Behavior of a Sand. *Géotechnique* **1965**, *15*, 32–56. [CrossRef]
23. Been, K.; Jefferies, M.; Hachey, J. The critical state of sands. *Géotechnique* **1991**, *41*, 365–381. [CrossRef]
24. Hardin, B.O.; Richart, F.E. Elastic Wave Velocities in Granular Soils. *J. Soil Mech. Found. Div.* **1963**, *83*, 33–65. [CrossRef]
25. Menq, F.-Y. Dynamic Properties of Sandy and Gravelly Soils. Ph.D. Thesis, University of Texas, Austin, TX, USA, 2003.
26. Payan, M.; Khoshghalb, A.; Senetakis, K.; Khalili, N. Small-strain stiffness of sand subjected to stress anisotropy. *Soil Dyn. Earthq. Eng.* **2016**, *88*, 143–151. [CrossRef]
27. Cascante, G.; Santamarina, J.C. Interparticle Contact Behaviour and Wave Propagation. *J. Geotech. Eng.* **1996**, *122*, 831–839. [CrossRef]
28. Saxena, S.K.; Reddy, R.K. *Mechanical Behavior of Cemented Sands*; IIT-CE-8701; Illinois Institute of Technology: Chicago, IL, USA, 1987.
29. Kostas, S.; Anastasiadis, A.; Pitilakis, K. The Small-Strain Modulus and Damping Ratio of Quartz and Volcanic Sands. *Geotech. Test. J.* **2012**, *35*, 1–17. [CrossRef]
30. Payan, M.; Senetakis, K.; Khoshghalb, A.; Khalili, N. Characterization of the small-strain dynamic behaviour of silty sands; contribution of silica non-plastic fines content. *Soil Dyn. Earthq. Eng.* **2017**, *102*, 232–240. [CrossRef]
31. Sadrekarimi, A.; Olson, S.M. The Importance of Mineralogy and Grain Compressibility in Understanding Field Behavior of Failures. In Proceedings of the International Conference on Case Histories in Geotechnical Engineering, Arlington, VA, USA, 11–16 August 2008.
32. Shin, H.; Santamarina, J.C. Role of Particle Angularity on the Mechanical Behaviour of Granular Mixtures. *J. Geotech. Geoenviron. Eng.* **2013**, *139*, 353–355. [CrossRef]
33. Sharma, A.; Leib-Day, A.R.; Thakur, M.M.; Penumadu, D. Effect of Particle Morphology on Stiffness, Strength and Volumetric Behavior of Rounded and Angular Natural Sand. *Materials* **2021**, *14*, 3023. [CrossRef]
34. Zheng, Y.; Wang, S.; Ziyuan, O.; Yongilao, Z.; Jiamzhong, L.; Chunlai, L.; Jumming, F. CAS-1 lunar soil simulant. *Adv. Space Res.* **2009**, *43*, 448–454. [CrossRef]
35. Isachenkov, M.; Chugunov, S.; Landsman, Z.; Akhatov, I.; Metke, A.; Tikhonov, A.; Shishkovsky, I. Characterization of novel lunar highland and mare simulants for ISRU research applications. *Icarus* **2022**, *376*, 114873. [CrossRef]
36. *JIS R 5201*; Physical Testing Methods for Cement. Japanese Standards Association: Tokyo, Japan, 2015.
37. Brown, J.M.; Angel, R.J.; Ross, N.L. Elasticity of plagioclase feldspars. *J. Geophys. Res. Solid Earth* **2016**, *121*, 663–675. [CrossRef]


https://doi.org/10.3390/aerospace13060527

38. Zhang, X.C. Lunar Regolith Simulant Behavior Affected by Shock Metamorphism and Minerology. Master's Thesis, University of Western Ontario, London, ON, Canada, 2021.
39. *ASTM D6913/D6913M-17*; Standard Test Methods for Particle-Size Distribution (Gradation) of Soils Using Sieve Analysis. ASTM International: West Conshohocken, PA, USA, 2017. [CrossRef]
40. *ASTM D7928-17*; Standard Test Method for Particle-Size Distribution (Gradation) of Fine-Grained Soils Using the Sedimentation (Hydrometer) Analysis. ASTM International: West Conshohocken, PA, USA, 2017. [CrossRef]
41. *ASTM D854-14*; Standard Test Methods for Specific Gravity of Soil Solids by Water Pycnometer. ASTM International: West Conshohocken, PA, USA, 2014. [CrossRef]
42. *ASTM D4253-16*; Standard Test Methods for Maximum Index Density and Unit Weight of Soils Using a Vibratory Table. ASTM International: West Conshohocken, PA, USA, 2016.
43. *ASTM D4254-16*; Standard Test Methods for Minimum Index Density and Unit Weight of Soils and Calculation of Relative Density. ASTM International: West Conshohocken, PA, USA, 2016.
44. *ASTM D3080-23*; Standard Test Method for Direct Shear Test of Soils Under Consolidated Drained Conditions. ASTM International: West Conshohocken, PA, USA, 2023. [CrossRef]
45. *ASTM D2435-20*; Standard Test Methods for One-Dimensional Consolidation Properties of Soils Using Incremental Loading. ASTM International: West Conshohocken, PA, USA, 2020. [CrossRef]
46. *ASTM D2487-17*; Standard Practice for Classification of Soils for Engineering Purposes (Unified Soil Classification System). ASTM International: West Conshohocken, PA, USA, 2017. [CrossRef]
47. Santamarina, J.C.; Cho, G.C. Soil behaviour: The role of particle shape. In *Advances in Geotechnical Engineering: The Skempton Conference*; Emerald Publishing Limited: Leeds, UK, 2004. [CrossRef]
48. Carrier, D.; Olhoeft, G.; Mendell, W. Physical Properties of the Lunar Surface. In *Lunar Sourcebook: A User's Guide to the Moon*; Heiken, G., Vaniman, D., Eds.; Cambridge University Press: Cambridge, UK, 1991; pp. 475–594.
49. Thannasi, P.; Muthukkumaran, K.; Indaram, V. Assessment of geotechnical properties of lunar simulants for lunar missions. *Indian J. Eng. Mater. Sci.* **2021**, *28*, 317–329.
50. Colin, S. Static and Dynamic Response of Silty Toyoura Sand with PVA Fiber and Cement Additives. Ph.D. Thesis, University of Western Ontario, London, ON, Canada, 2015.
51. Goguen, J.; Sharits, A.; Chiaramonti, A.; Lafarge, T.; Garboczi, E. Three-dimensional characterization of particle size, shape and internal porosity for Apollo 11 and Apollo 14 lunar regolith and JSC-1A lunar regolith soil simulant. *Icarus* **2024**, *420*, 116166. [CrossRef]
52. Tsuchiyama, A.; Sakurama, T.; Nakano, T.; Uesugi, K.; Ohtake, M.; Matsushima, T.; Terakado, K.; Galimov, E.M. Three-dimensional shape distribution of lunar regolith particles collected by the Apollo and Luna programs. *Earth Planets Space* **2022**, *74*, 172. [CrossRef]
53. Manmatharajan, M.V.; Gill, S.; Liu, W.; Ingabire, E.-P.; Sy, A.; Ghafghazi, M. Effect of particle size and particle size distribution on critical state loci of granular soils. *Can. Geotech. J.* **2023**, *60*, 1117–1131. [CrossRef]
54. Kwa, K.; Airey, D. Critical state interpretation of effects of fines in silty sands. *Geotech. Lett.* **2016**, *6*, 100–105. [CrossRef]
55. Soares, M.; Fonseca, A. Factors Affecting Steady State Locus in Triaxial Tests. *Geotech. Test. J.* **2016**, *39*, 1056–1078. [CrossRef]
56. Cho, G.-C.; Dodds, J.; Santamarina, J.C. Particle Shape Effects on Packing Density, Stiffness and Strength: Natural and Crushed Sands. *J. Geotech. Geoenviron. Eng.* **2006**, *132*, 591–602. [CrossRef]
57. Ahmed, S.; Martinez, A.; DeJong, J. Gradation and state effects on the strength and dilatancy of coarse-grained soils. In Proceedings of the Deformation Characteristics of Geomaterials, Porto, Portugal, 3–6 September 2023.
58. Youd, T. Factors Controlling Maximum and Minimum Densities of Sand. *ASTM Spec. Tech. Publ.* **1973**, *525*, 98–112.
59. de Bono, J.D.; McDowell, G.R. Investigating the effects of particle shape on normal compression and overconsolidation using DEM. *Granul. Matter* **2016**, *18*, 55. [CrossRef]
60. Pino, L.F.M.; Baudet, B.A. The effect of particle size distribution on the mechanics of fibre-reinforced sands under one-dimensional compression. *Geotext. Geomembr.* **2015**, *43*, 250–258. [CrossRef]
61. Schofield, A.N.; Wroth, P. *Critical State Soil Mechanics*; McGraw-Hill: London, UK, 1968.
62. Rowe, P.W. The stress–dilatancy relation for static equilibrium of an assembly of particles in contact. *Proc. R. Soc. A* **1962**, *269*, 500–527. [CrossRef]
63. Lee, K.L.; Seed, H.B. Drained Strength Characteristics of Sands. *J. Soil Mech. Found. Div.* **1967**, *93*, 117–141. [CrossRef]
64. Peck, R.B.; Mesri, G. *Soil Mechanics in Engineering Practice*; Wiley: New York, NY, USA, 1996.
65. Barrett, P. The shape of rock particles: A critical review. *Sedimentology* **1980**, *27*, 291–303. [CrossRef]
66. Been, K.; Jefferies, M. A state parameter for sands. *Géotechnique* **1985**, *35*, 99–112. [CrossRef]
67. Wan, R.; Guo, P. A Pressure and Density Dependent Dilatancy Model for Granular Materials. *Soils Found.* **1999**, *39*, 1–11. [CrossRef]

68. Dietz, M.S.; Lings, M.L. Postpeak strength of interfaces in a stress-dilatancy framework. *J. Geotech. Geoenviron. Eng.* **2006**, *132*, 1474–1484. [CrossRef]
69. Sture, S.; Costes, N.C.; Batiste, S.N.; Lankton, M.R.; Alshibli, K.A.; Jermic, B.; Swanson, R.A.; Frank, M. Mechanics of Granular Materials at Low Effective Stresses. *J. Aerosp. Eng.* **1998**, *11*, 67–72. [CrossRef]
70. Casagrande, A. The determination of the pre-consolidation load and its practical significance. In Proceedings of the 1st International Conference on Soil Mechanics and Foundation Engineering, Cambridge, MA, USA, 22–26 June 1936.
71. Coulomb, C. *Essai sur une Application des Règles de Maximis et Minimis à Quelques Problèmes de Statique, Relatifs à L'architecture*; Imprimerie Royale: Paris, France, 1776.
72. Mohr, O. Welche Umstande bedingen die Elastizitatsgrenze und den Bruch eines Materials? *Z. Ver. Dtsch. Ing.* **1900**, *44*, 1524–1530.
73. Sadrekarimi, A.; Olson, S. Critical state friction angle of sands. *Géotechnique* **2011**, *61*, 771–783. [CrossRef]
74. Papike, J.; Simon, S.; Laul, J. The lunar regolith: Chemistry, mineralogy, and petrology. *Rev. Geophys.* **1982**, *20*, 761–826. [CrossRef]
75. Morris, R.V.; Klingelhöfer, G.; Korotev, R.L.; Shelfer, T.D. Mössbauer mineralogy on the Moon: The lunar regolith. *Hyperfine Interact.* **1998**, *117*, 405–432. [CrossRef]
76. Yang, X.; Desai, C.S. General Stress–Dilatancy Relation for Granular Soils. *J. Geotech. Geoenviron. Eng.* **2016**, *142*. [CrossRef]
77. Bolton, M. The strength and dilatancy of sands. *Géotechnique* **1986**, *36*, 65–78. [CrossRef]
78. Simoni, A.; Houlsby, G.S. The Direct Shear Strength and Dilatancy of Sand–Gravel Mixtures. *Geotech. Geol. Eng.* **2006**, *24*, 523–549. [CrossRef]
79. Taylor, D.W. *Fundamentals of Soil Mechanics*; Wiley: New York, NY, USA, 1948.
80. Stroud, M.A. Sand at Low Stress Levels in the Simple Shear Apparatus. Ph.D. Thesis, University of Cambridge, Cambridge, UK, 1971.
81. Tanghetti, G.; Davies, M.C.; Goodey, R. Comparison small and full scale of shear box tests on large particle size aggregate. In Proceedings of the Conference on Soil Mechanics and Geotechnical Engineering, Sydney, Australia, 1–5 May 2022.
82. Vaid, Y.P.; Byrne, P.M.; Hughes, J.M. Dilation Angle and Liquefaction Potential. *J. Geotech. Eng. Div.* **1981**, *107*, 1003–1008. [CrossRef]
83. Chakraborty, T.; Salgado, R. Dilatancy and shear strength of sand at low confining pressures. *J. Geotech. Geoenviron. Eng.* **2010**, *136*, 527–532. [CrossRef]
84. Shoemaker, E.; Batson, R.; Holt, H.; Morris, E.; Rennilson, J.; Whitaker, E. Observations of lunar regolith and the Earth from the television camera on Surveyor 7. *J. Geophys. Res.* **1969**, *74*, 6081–6119. [CrossRef]
85. Melosh, H.J. *Planetary Surface Processes*; Cambridge University Press: Cambridge, UK, 2011.
86. Zacny, K.; Wilson, J.; Craft, J.; Asnani, V.; Oravec, H.; Creager, C.; Johnson, J.; Fong, T. Robotic lunar geotechnical tool. In Proceedings of the Earth and Space Conference, Honolulu, HI, USA, 14–17 March 2010.
87. Colwell, J.; Batiste, S.; Horányi, M.; Robertson, S.; Sture, S. Lunar surface: Dust dynamics and regolith mechanics. *Rev. Geophys.* **2007**, *45*. [CrossRef]
88. Pirrone, S.R.; Witchalls, J.; Dillenburger, J.; Patil, T.; Castro, A.C.; Hadler, K. Lunar Regolith Sampling Technologies: A Critical Review. *Space Sci. Rev.* **2025**, *221*, 111. [CrossRef]
89. Horz, F.; Grieve, R.; Heiken, G.; Spudis, P.; Binder, A. Lunar Surface Processes. In *Lunar Sourcebook: A User's Guide to the Moon*; Heiken, G., Vaniman, D., Eds.; Cambridge University Press: Cambridge, UK, 1991; pp. 61–120.
90. Bareither, C.A.; Benson, C.H.; Edil, T.B. Comparison of shear strength of sand backfills measured in small-scale and large-scale direct shear tests. *Can. Geotech. J.* **2008**, *45*, 1224–1236. [CrossRef]
91. Mitchell, J.K.; Houston, W.N.; Scott, R.F.; Costes, N.C.; Carrier, W.D.; Bromwell, L.G. Mechanical properties of lunar soil: Density, porosity, cohesion, and angle of internal friction. In Proceedings of the Third Lunar Science Conference, Houston, TX, USA, 10–13 January 1972.
92. Liu, S.; Shao, L.; Li, H. Slope stability analysis using the limit equilibrium method and two finite element methods. *Comput. Geotech.* **2015**, *63*, 291–298. [CrossRef]
93. Huang, Y.; Zhang, J.; Li, B.; Chen, S. Slope Stability Analysis and Soil Mechanical Properties of Impact Craters around the Lunar South Pole. *Remote Sens.* **2024**, *16*, 371. [CrossRef]
94. Jiang, S.; Hu, H.; Wang, Z. Improved Bayesian model updating of geomaterial parameters for slope reliability assessment considering spatial variability. *Struct. Saf.* **2025**, *112*, 102536. [CrossRef]
95. Terzaghi, K. *Theoretical Soil Mechanics*; Wiley: New York, NY, USA, 1943.
96. Vesic, A.S. Analysis of Ultimate Loads of Shallow Foundations. *J. Soil Mech. Found. Div.* **1973**, *99*, 45–73. [CrossRef]
97. Loukidis, D.; Salgado, R. Bearing capacity of strip and circular footings in sand using finite elements. *Comput. Geotech.* **2009**, *36*, 871–879. [CrossRef]
98. Perkins, S.; Madson, C. A dilatancy approach for bearing capacity of sand. In Proceedings of the Soil Mechanics and Foundation Engineering, Hamburg, Germany, 6–12 September 1997.

99. Oravec, H.A.; Phillip, A.B. Simulated Lunar Environment for the Study of Regolith Strength. In Proceedings of the Dayton/Cincinnati Aerospace Sciences Symposium, Miamisburg, OH, USA, 6 March 2012.
100. Mesri, G.; Vardhanabhuti, B. Compression of granular materials. *Can. Geotech. J.* **2009**, *46*, 369–392. [CrossRef]
101. Bolton, M.D. Discussion: The strength and dilatancy of sands. *Géotechnique* **1987**, *37*, 219–226. [CrossRef]
102. Conte, E.; Donato, A.; Troncone, A. Progressive failure analysis of shallow foundations on soils with strain-softening behaviour. *Comput. Geotech.* **2013**, *54*, 117–124. [CrossRef]
103. Loukidis, D.; Chakraborty, T.; Salgado, R. Bearing capacity of strip footings on purely frictional soil under eccentric and inclined loads. *Can. Geotech. J.* **2008**, *45*, 768–787. [CrossRef]
104. Bishop, A.W.; Henkel, D.J. *The Measurement of Soil Properties in the Triaxial Test*; Edward Arnold: London, UK, 1957.
105. Scarpelli, G.; Wood, D.M. Experimental observation of shear patterns in direct shear tests. In Proceedings of the Deformation and Failure of Granular Materials, Delft, The Netherlands, 31 August–3 September 1982.
106. Hanna, A.; Ayadat, T. Comparative study of shear strength characteristics of dry cohesionless sands from triaxial, plane-strain and direct shear tests. *Geomech. Geoeng.* **2019**, *16*, 150–162. [CrossRef]
107. Boussinesq, J. *Applications des Potentials à L'étude de L'équilibre et du Movement des Solides Élastique*; Gauthier-Villars: Paris, France, 1885.
108. Leone, G.; Ahrens, C.; Korteniemi, J.; Gasparri, D.; Kereszturi, A.; Martynov, A.; Schmidt, G.; Calabrese, G.; Joutsenvaara, J. Sverdrup-Henson crater: A candidate location for the first lunar South Pole settlement. *iScience* **2023**, *26*, 107853. [CrossRef]




https://doi.org/10.3390/aerospace13060527